RESEARCH ARTICLE

Open Access

Abrupt water temperature increases near seafloor during the 2011 Tohoku earthquake

Daisuke Inazu[1]* , Yoshihiro Ito[2], Ryota Hino[3] and Wataru Tanikawa[4]

Abstract

We investigated temperature records associated with seafloor pressure observations at eight stations that experienced the 2011 M_w 9 Tohoku earthquake near its epicenter. The temperature data were based on the temperature measured inside the pressure transducer. We proposed a method to estimate ambient water temperature from the internal temperature using an equation of heat conduction. The estimated seafloor water temperature showed remarkable anomalies, especially increases several hours after the M_w 9 earthquake. A station of P03 (sea depth of 1.1 km) showed an abrupt temperature increase of $+0.19$ °C that occurred ~3 h after the earthquake, which lasted for several hours. At stations of GJT3 (sea depth of 3.3 km) and TJT1 (sea depth of 5.8 km), there were abrupt temperature anomalies of $+0.20$ °C and $+0.10$ °C that began to occur 3–4 h after the earthquake. These anomalies both decayed to their original levels over a few tens of days. During the decay processes, only TJT1 showed several intermittent temperature rises. A water temperature anomaly within $+0.03$ °C was found up to ~500 m above TJT1 2 weeks after the earthquake. There was no significant anomaly at the other five stations. Processes to cause these seafloor temperature anomalies were discussed. The temperature anomaly of P03 was reasonably caused by a tsunami-generated turbidity current, as also suggested by a previous study. Meanwhile, we proposed a scenario that the abrupt temperature anomalies of GJT3/TJT1 and the intermittent anomalies of TJT1 were caused by warm water discharges from the subseafloor. The pathways of the warm water were probably composed of the branch normal fault between GJT3 and TJT1, the reverse fault near TJT1, the backstop interface, and perhaps reverse faults at the frontal prism. The proposed scenario was almost compatible with other studies based on epicentral observations. We estimated the heat properties of the initial temperature anomalies of GJT3/TJT1. The estimated heat source might be explained by that most of the geothermal fluids trapped in those fault pathways were discharged to the seafloor immediately after the earthquake. The onsets of the subsequent intermittent anomalies of TJT1 were possibly activated by low or falling ocean tidal loading.

Keywords Seafloor temperature, Seafloor pressure, 2011 Tohoku earthquake, Water temperature increase, Built-in thermometer, Ambient water temperature, Vertical structure of water temperature, Warm water discharge, Subseafloor fluid, Turbidity current

*Correspondence:
Daisuke Inazu
inazud@kaiyodai.ac.jp
Full list of author information is available at the end of the article

Inazu *et al. Progress in Earth and Planetary Science* (2023) 10:24

Page 2 of 27

1 Introduction

A moment magnitude (M_w) 9 earthquake, called the 2011 Tohoku earthquake, occurred below a landward slope of the Japan Trench on March 11, 2011. A M_w 7 earthquake (hereafter foreshock) occurred 2 days prior to the M_w 9 earthquake (hereafter mainshock). The mainshock was followed by numerous distinct aftershocks. The slip distribution and tsunami due to the mainshock were quickly estimated using data derived from established onshore/offshore observations of the seismic waves, crustal deformation, and tsunami (e.g., Suzuki et al. 2011; Iinuma et al. 2011; Fujii et al. 2011). Advanced marine observations near the epicenter revealed not only the earthquake and tsunami but also various environmental disturbances. The observations included continuous and repeating geophysical surveys before and after the mainshock, as well as geochemical and geological surveys quickly carried out after the mainshock.

We carried out continuous seafloor pressure observations above the hypocenter (Hino et al. 2014). The pressure sensors experienced the mainshock (Fig. 1a) and successfully recorded the seismic waves, seafloor crustal deformation, and tsunami with fine temporal resolution and large amplitude range (Hino et al. 2013, 2014). These data have enabled detailed estimation and modeling of the earthquake and tsunami (e.g., Saito et al. 2011; Iinuma et al. 2012; Dettmer et al. 2016; Kubota et al. 2021).

Repeating geophysical observations identified large seafloor deformation due to the mainshock. Horizontal seafloor displacements of tens of meters near the Japan Trench were found by an established acoustic seafloor geodetic survey (Kido et al. 2011). Repeating seismic exploration surveys found a large slump failure close to the trench axis (Kodaira et al. 2012). Using seafloor heat-flow measurements months after the mainshock and referring to seismic exploration surveys, Tsuji et al. (2013) suggested that a distinct branch normal fault was activated by anelastic extensional deformation due to the larger slip closer to the trench axis and substantial heat was then discharged from the subseafloor. These geophysical surveys were mostly carried out along a repeatedly investigated cross section of MY102 (Fig. 1b) in which seismic explorations have clearly identified the branch normal fault, the backstop interface, the frontal prism, and so on (e.g., Tsuru et al. 2002; Miura et al. 2005; Tsuji et al. 2011; Kodaira et al. 2017, 2020).

Temporal observations near the epicenter quickly carried out after the mainshock revealed remarkable marine environmental disturbances. The Japan Agency for Marine-Earth Science and Technology (JAMSTEC) played an important role in the urgent cruise using the research vessel (R/V) *Mirai* (MR11-03), which was successfully carried out ~1 month after the mainshock. The cruise conducted water sampling with conductivity–temperature–depth (CTD) profilers and examined relevant water properties above the epicentral region near the seafloor pressure observations and the MY102 section. Several results were reported based on the measured data and samples.

Kawagucci et al. (2012) examined a carbon isotope ratio ($^{13}C/^{12}C$) of methane in the seawater sampled 36 days after the mainshock and suggested that methane at ~1 km below seafloor (Ijiri et al. 2009) was discharged along the branch normal fault (Tsuji et al. 2011). Sano et al. (2014) examined a helium isotope ratio ($^{3}He/^{4}He$) in the seawater samples and suggested that subseafloor fluids with mantle-derived ^{3}He were emitted from the seafloor after the mainshock. According to Park et al. (2021), seismic exploration and tomography results after the mainshock imaged seismic-wave low-velocity regions at depths deeper than ~10 km, including the branch normal fault and clear reflection boundaries at the shallower subseafloor, which suggested that the branch normal fault was a possible migration pathway of the fluids with the $^{3}He/^{4}He$ anomaly.

Noguchi et al. (2012) observed vertical distributions of water turbidity 36 days after the mainshock and revealed that the water turbidity anomaly was higher near deeper seafloor (e.g., turbidity anomaly extended to ~1.5 km above the seafloor of 5.7 km). They suggested that the turbidity anomaly was mainly induced by a remarkable landslide close to the trench axis identified by Fujiwara et al. (2011). The landslide was reinterpreted as a slump failure by Kodaira et al. (2012) and Strasser et al. (2013). Four months after the mainshock, Oguri et al. (2013) carried out other turbidity surveys which were similar to those of Noguchi et al. (2012). They measured vertical distributions of turbidity at sea depths of 7.3 and 7.5 km, just above the trench axis, and detected turbidity anomalies extended 30 and 50 m above the seafloor, respectively.

Five months after the mainshock, Usami et al. (2017) and Ikehara et al. (2021) sampled seafloor sediments at depths up to ~4 km off Miyagi (Fig. 1a). They also investigated sediments stuck in the plastic cases of seafloor instruments that experienced the mainshock (Arai et al. 2013; Miura et al. 2014) and discussed disturbances of seafloor sediments induced by the mainshock. They suggested that there were almost short-distance (e.g., < ~1 km) lateral transports of suspended sediments due to disturbances from the tsunami, landslide, and strong ground motion. Very few exceptional long-distance (e.g., > 10 km) transports of suspended sediments were induced by the tsunami-generated turbidity current, which involved a self-accelerating mechanism (Arai et al.
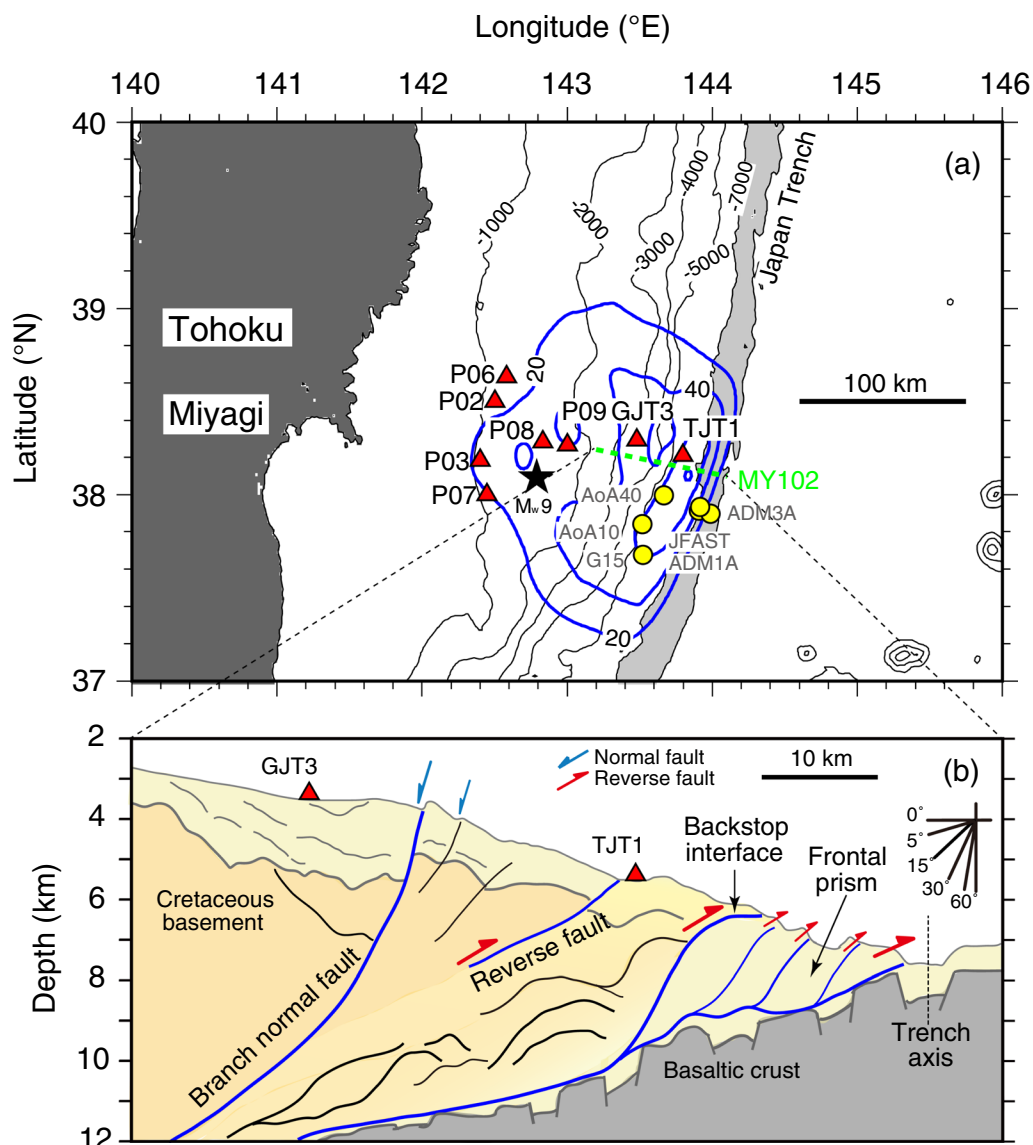
Fig. 1 a Locations of seafloor pressure gauges and **b** subseafloor structure along the MY102 section. In **a** red triangles denote the seafloor gauges that recorded the 2011 M_w 9 Tohoku earthquake (its epicenter denoted by a star), and yellow circles denote the deep-sea observations conducted after the earthquake (Table 1). An estimated coseismic slip distribution (Iinuma et al. 2012) of 20, 40, and 60 m is indicated by blue contours. In **b** the seafloor stations of TJT1 and GJT3 near MY102 are projected. The MY102 section is based on Tsuji et al. (2013). Distinct fault boundaries are traced by blue curves

2013). The short-distance lateral transports of suspended sediments indicated that the suspended sediments were redeposited near their original positions. Redepositions were also identified at sea depths of 5–7 km with steep slopes close to the trench axis off Miyagi (e.g., Ikehara et al. 2016; McHugh et al. 2016, 2020).

Although the respective temporal observations could capture snapshots of marine environmental disturbances, it has been still difficult to elucidate dynamic behaviors of the disturbances during the mainshock with fine

temporal resolution. In this paper, we again focus on the seafloor pressure observations which recorded the 2011 M_w 9 earthquake near its epicenter (Hino et al. 2013, 2014). In particular, the records of a thermometer in the pressure gauge are investigated in detail. Since the built-in thermometer does not strictly record the ambient temperature around the instrument, this study proposes a method to reasonably estimate ambient water temperature from the built-in thermometer data. By the proposed method, we reconstruct seafloor water

Inazu *et al. Progress in Earth and Planetary Science* (2023) 10:24

Page 4 of 27

temperature variations including the period during the M_w 9 earthquake in which there was no other explicit water temperature information. As a result, we demonstrate that there were remarkable water temperature anomalies, especially increases, after the mainshock. We rigorously discuss processes that caused the temperature increases and propose a scenario to explain the temperature increases. The scenario is confirmed to be compatible with the results of the geophysical, geochemical, and geological investigations mentioned above. We also discuss the heat content and source which induced the temperature increases.

2 Data and methods

2.1 Temperature recording in the pressure measurement

The Digiquartz® pressure sensor employing a quartz-crystal oscillator manufactured by Paroscientific, Inc., was used for the absolute pressure measurement. We installed the pressure sensor to a self-floating, glass-sphere system to observe the absolute pressure at the seafloor. Such a stand-alone observation system has been applied to many geophysical surveys (e.g., Eble and Gonzalez 1991; Nooner and Chadwick 2009; Macrander et al. 2010; Fujimoto 2014). To accurately measure the absolute pressure, the temperature of the pressure oscillator attached to a Bourdon tube in the enclosure was measured by another quartz-crystal oscillator (i.e., built-in thermometer) for the thermal compensation of the pressure oscillator (Eble et al. 1989; Yilmaz et al. 2004). Although the temperature recorded by the built-in thermometer (hereafter, internal temperature) is not strictly the ambient temperature, some studies somehow utilized the internal temperature as a proxy of the ambient water temperature at the seafloor (e.g., Fox 1999; Chadwick et al. 2012; Johnson et al. 2017).

We have repeatedly carried out seafloor pressure observations at the landward slope of the Japan Trench since before the 2011 Tohoku earthquake (Hino et al. 2009, 2014). A ship goes above an observation site to deploy a seafloor pressure gauge or retrieve another instrument. Each measurement has been performed for approximately one year due to a constraint of the observation system. In addition to the data when the pressure gauge stays at the seafloor, we attempt to utilize the temperature records during the deployment (i.e., free fall to the seafloor) and retrieval (i.e., anchor detachment and floating up to the sea surface) to obtain vertical distributions of the seawater temperature and to find possible temperature anomalies above the pressure gauge. The internal temperature data during the deployment and retrieval have not been usually used. For the stand-alone pressure observation system (Hino et al. 2009, 2014; Fujimoto

2014), the vertical speeds of the pressure gauge during free falling and floating up in the ocean have been almost designed to be 1.1–1.4 m/s and 0.8–1.2 m/s, respectively.

We recovered the data from eight stations at sea depths of 1.1–5.8 km, which recorded the 2011 Tohoku earthquake (Hino et al. 2013; Fujimoto et al. 2014). Other observations at eight stations at sea depths of 5.1–7.3 km were conducted after the earthquake, and their data are used to evaluate the vertical structure of water temperature above the epicentral region (Fig. 1 and Table 1). Our data recording systems except for TJT1 were capable of up to a 1-s sampling measurement and could sensitively record high-frequency (up to ~1 cycle per second) pressure variations without significant mechanical damping (e.g., Webb and Nooner 2016; Kubota et al. 2021). Only TJT1 employed a system by a 30-s sampling measurement. It is necessary to take care of the clock accuracy of stand-alone measurement systems. We corrected the clock drift of the recorder by linear interpolation based on the time difference between the internal clock and the GPS clock measured when the instrument was recovered after the observation. The corrected time stamps of the pressure and internal temperature overall had accuracy within a second.

2.2 Estimation of ambient water temperature

To examine the relationship between the internal temperature and the ambient water temperature, we attached a stand-alone external water temperature sensor manufactured by RBR Ltd. (TR-1050) to a seafloor pressure gauge and conducted a 1-year observation (SBPR-2) at the Hikurangi Trough, offshore New Zealand (Table 1). Meanwhile, we carried out preliminary seafloor observations that multiple TR-1050 sensors were redundantly attached to a seafloor pressure gauge (Suzuki et al. 2015), which was used to evaluate the accuracy of TR-1050 sensors, especially the clock accuracy and the accuracy of recorded temperature values. We then confirmed that the TR-1050 sensor involved clock drifts within ~1 min/year and temperature accuracy within ~0.01 °C. Since we did not correct the clock drift of the external thermometer (TR-1050), the time difference between the internal and the external temperature might be up to ~1 min at the latter period of the observation.

Figure 2 shows the temperature recording of the built-in thermometer and the water temperature recorded by the external water temperature sensor. The correlation coefficient between them was 0.96 (Fig. 2a), which means that the built-in thermometer well captured the ambient water temperature. Meanwhile, the internal temperature showed a deviation of the mean value of 0.50 °C from the external water temperature sensor. For the absolute value of the temperature, we trust the external water temperature

Table 1 List of seafloor pressure/temperature data used in this study

Station	Latitude (°N)	Longitude (°E)	Sea depth (m)	Model	Install (yyyy-mm-dd)	Float up (yyyy-mm-dd)	Note
TJT1	38.2094	143.7958	5771	8B7000	2010-04-07	2011-03-24	
TJT1-2	38.2090	143.7886	5760	8B7000	2011-04-30	2011-05-24	
GJT3	38.2945	143.4814	3293	8B7000	2010-11-12	2011-05-31	
P09	38.2650	143.0002	1556	8B7000	2010-09-28	2011-09-25	ROV salvage
P08	38.2829	142.8320	1418	8B7000	2010-09-27	2011-09-25	ROV salvage
P06	38.6340	142.5838	1254	8B7000	2010-06-23	2011-05-26	
P02	38.5002	142.5016	1104	8B7000	2010-06-21	2011-05-26	
P03	38.1834	142.3998	1052	8B7000	2010-06-21	2011-09-24	ROV salvage
P07	38.0016	142.4495	1059	8B7000	2010-09-27	2011-09-25	ROV salvage
ADM3A	37.8983	143.9883	7249	8B7000	2015-09-23	2016-09-23	
ADM1A	37.9135	143.9091	6903	8B7000	2015-09-23	2016-09-23	
JFAST-1	37.9384	143.8728	6482	8B7000	2012-05-20	2012-10-06	
JFAST-2	37.9336	143.9154	6799	8CB7000-I-005	2012-10-06	2013-05-18	
AoA40	37.9975	143.6668	5440	8B7000	2015-09-23	2016-10-03	
G15	37.6771	143.5214	5262	8B7000	2015-09-25	2016-09-19	
AoA10b	37.8416	143.5169	5054	8B7000	2015-09-25	2016-09-19	
SBPR-2	− 38.8474	178.8752	2116	8B4000-I	2014-05-12	2015-06-23	New Zealand

sensor since its accuracy is almost within ∼ 0.01 °C as mentioned above. The temperature offset was likely due to that the internal temperature might be insufficiently calibrated since the internal temperature is intended to be used for the thermal correction of the pressure oscillator. Thus, the internal temperature well reflects variations of the ambient water temperature although its absolute value may not be so reliable.

Note that the internal temperature variation lagged behind the ambient water temperature by ∼ 15 min (Fig. 2a and c). Figure 2b indicates that the internal temperature showed a smaller amplitude than the ambient temperature at high frequency ($> 10^{-2}$ cycles per minute). Since the built-in thermometer measures the temperature at the quartz-crystal plate in the pressure transducer (e.g., Fig. 3 of Yilmaz et al. 2004 and Fig. 2 of Matsumoto and Araki 2021), the outside water temperature is likely attenuated as it is transmitted to the inside of the enclosure at high-frequency variations. The delay time almost depends on how well the enclosure is shielded. The delay time effect should be suitably corrected if the internal temperature sensor is used to accurately measure the ambient temperature.

We suppose that the process of transmitting outside ambient temperature (i.e., air or water temperature) to the inside of the enclosure is suitably modeled by a simplified equation of heat conduction (e.g., Lienhard and Lienhard 2003):

$$\frac{\mathrm{d}T_{\mathrm{O}}}{\mathrm{d}t} = -A(T_{\mathrm{O}} - T_{\mathrm{i}}) + \frac{\mathrm{d}T_{\mathrm{i}}}{\mathrm{d}t}, \tag{1}$$

where T_{o} and T_{i} are the ambient temperature and the internal temperature, respectively. A is a positive coefficient whose dimension is inverse of time, which is recognized as a decay time coefficient. When T_{o} is constant, the analytical solution of T_{i} is an exponential decay model. This equation is numerically solved, and the ambient temperature (T_{o}) can be estimated from the internal temperature (T_{i}). A fourth-order Runge–Kutta method is used for the numerical integration.

When the decay time is set to 25 min ($= A^{-1}$), the 15-min delay is mostly eliminated (Fig. 2c) and the correlation coefficient is improved to 0.98 between the ambient water temperature and the estimated temperature (Fig. 2a). According to the power and phase spectra of the estimated temperature (Fig. 2b, c), we understand that the proposed method works well to reconstruct the ambient water temperature at time scales greater than tens of minutes.

When $A^{-1} = 25$ min is applied, the vertical distribution of the ambient water temperature from the seafloor to the sea surface is also well traced by the estimation from the internal temperature (Fig. 3b). This indicates that the internal temperature records during the floating up of the pressure gauge can be used to successfully replicate a vertical distribution of the water temperature

Inazu *et al. Progress in Earth and Planetary Science* (2023) 10:24

Page 6 of 27
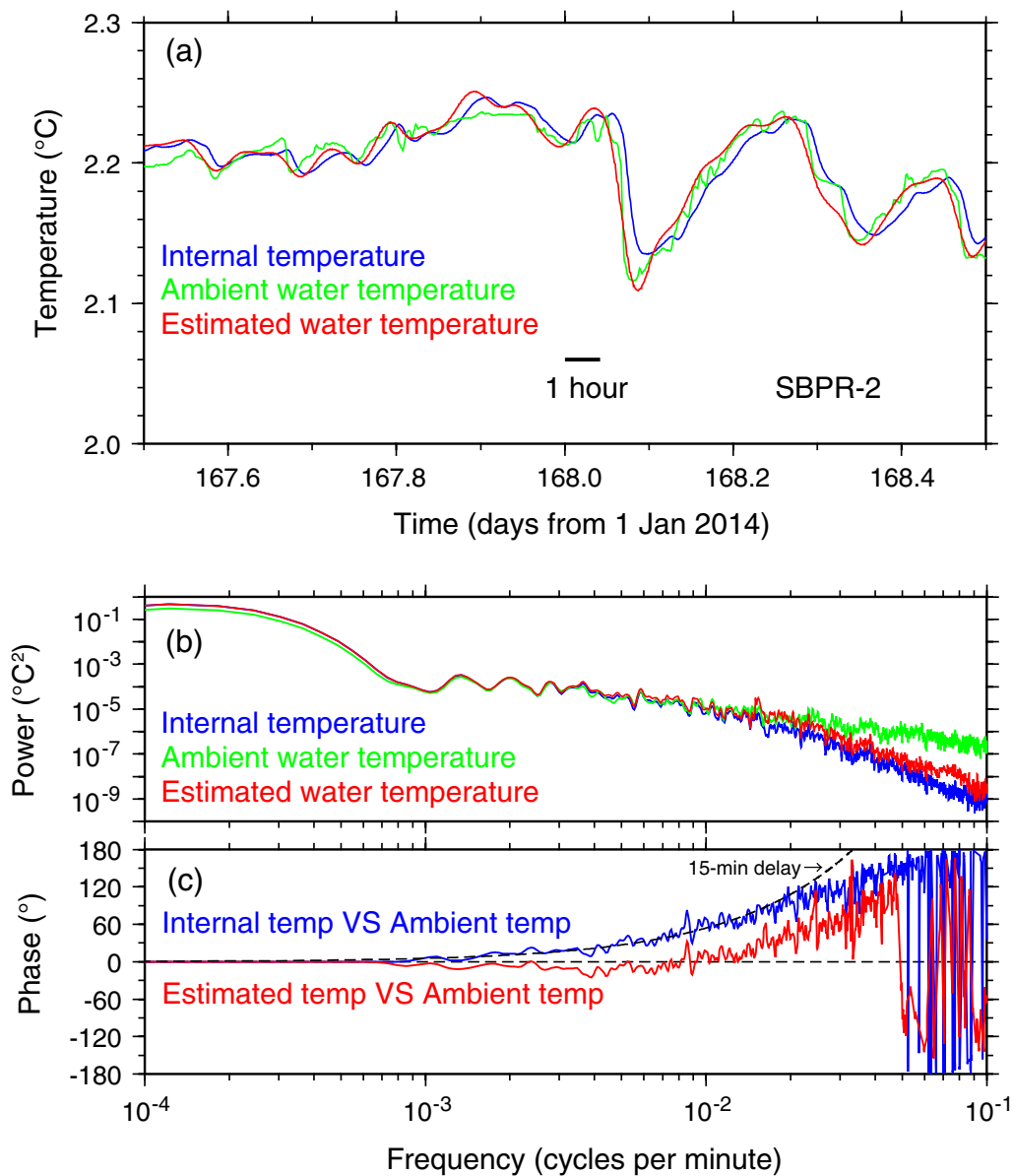
Fig. 2 **a** Time series, **b** power spectra, and **c** phase spectra of each temperature of SBPR-2 (Table 1). In **a** and **b** blue, green, and red curves denote internal temperature, ambient water temperature measured by an external thermometer, and water temperature estimated from the internal temperature, respectively. The internal temperature is shifted by –0.50 °C to meet the ambient water temperature. In **c**, phase differences are shown between the ambient temperature and (blue) the internal temperature, and (red) the estimated temperature, respectively. The positive phase means a delay from the ambient temperature. A 15-min delay from the ambient temperature is shown by a dashed curve. The phase spectra are shown when coherence-squared is greater than 0.6

by a CTD observation. However, when the equipment is falling from the sea surface to the seafloor, the vertical distribution of the water temperature could not be well estimated by at least applying a single decay time coefficient (Fig. 3a). It seemed also difficult to estimate ambient temperature when the equipment was drifting at the sea surface just before the picking up of the equipment although this is not important for our purpose (Fig. 3b).

We tried to apply other values of the decay time coefficient but failed to reconstruct the vertical distribution during the installation of the equipment.

We have assumed the decay time coefficient A is constant in Eq. (1). According to Lienhard and Lienhard (2003), A depends on the temperature difference between the ambient media and the inside of the
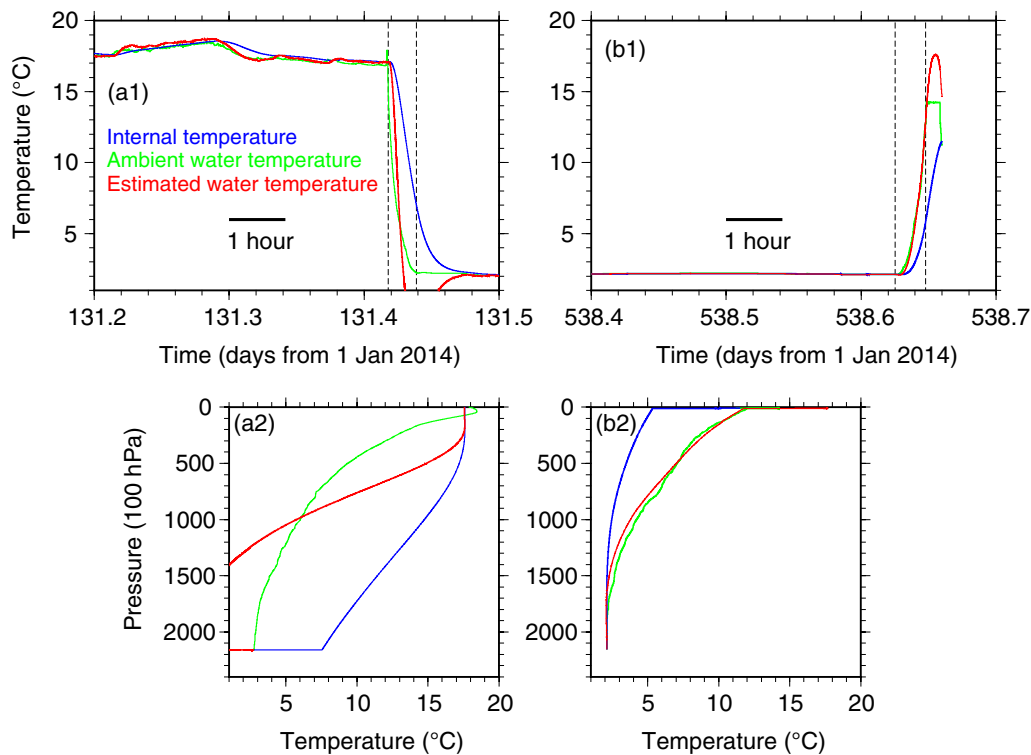
Fig. 3 Temperature changes along (upper: 1) time and (lower: 2) pressure or water depth during (left: **a**) falling down and (right: **b**) floating up of the equipment of SBPR-2. Blue, green, and red curves denote the internal temperature, the ambient (air or water) temperature, and the estimated water temperature, respectively. The internal temperature is shifted by $-0.50\ ^{\circ}$C as well as Fig. 2. Time windows between dashed lines in the upper panels indicate periods when the equipment is vertically moving

enclosure ($T_{\mathrm{O}} - T_{\mathrm{i}}$) and also depends on the thickness of the thermal boundary layer between the ambient media and the surface of the enclosure. We found that $|T_{\mathrm{O}} - T_{\mathrm{i}}|$ was relatively large ($>5\ ^{\circ}$C) during and after the equipment's passage through thermoclines near the sea surface (Fig. 3) although we implicitly assume that Eq. (1) is valid when $|T_{\mathrm{O}} - T_{\mathrm{i}}|$ is small enough. Since there is an order of magnitude difference in the kinematic viscosity coefficients of air and water, both the thermal boundary layer thickness and A substantially change when the media around the enclosure changes from air to water (i.e., releasing the equipment at sea surface) and from water to air (i.e., picking up the equipment from sea surface). The effect of the transient change likely continued to some extent. Those two factors would account for the failure of the temperature estimation when the equipment was falling from the sea surface and drifting at the sea surface.

When the equipment was staying on the seafloor and started to float up from the seafloor to the upper ocean after the long-time seafloor observation, $|T_{\mathrm{O}} - T_{\mathrm{i}}|$ was

small and the thermal boundary layer thickness around the enclosure was stable, which caused no change in A. Thus, it is reasonable that the ambient water temperature was successfully estimated by Eq. (1) during this period.

3 Results

3.1 Pressure and temperature of TJT1

Figure 4 shows the pressure and temperature records of TJT1 at a sea depth of 5.8 km. A large stepwise pressure decrease of ~ 500 hPa revealed a 5-m uplift of the seafloor below TJT1 due to the mainshock, which occurred on the Day of Year (DOY) 434.2403 or 05:46 UT on March 11, 2011 (Ito et al. 2011). The internal temperature and the ambient water temperature estimated by Eq. (1) are shown in Fig. 4b, c, respectively. An abrupt temperature increase of about $+0.10\ ^{\circ}$C was observed several hours after the mainshock. Meanwhile, the seafloor pressure of TJT1 and other stations at the epicentral region more quickly showed effects of the seismic vibration, vertical seafloor displacement, and tsunami within
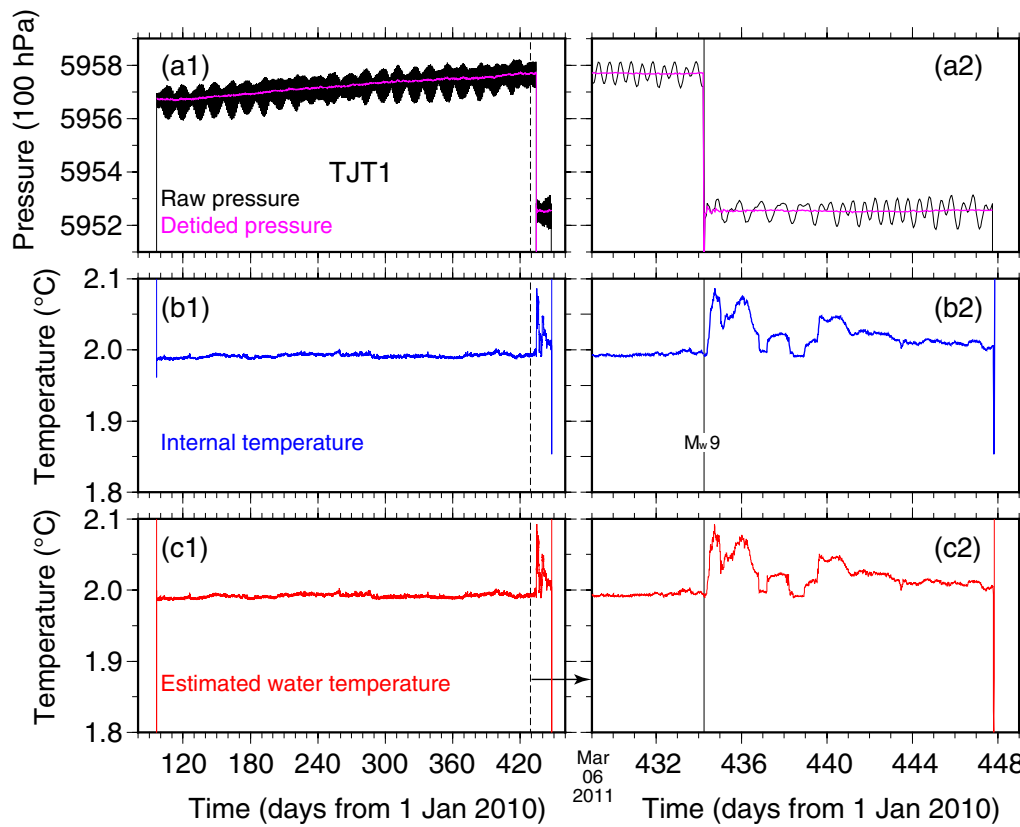
Fig. 4 Time series of **a** absolute pressure, **b** internal temperature, and **c** estimated water temperature of TJT1. Right panels show expanded time windows during DOY 429–449 (March 6–26, 2011), in which vertical lines indicate the M_w 9 earthquake occurrence time (DOY 434.2403 or 05:46 UT on March 11, 2011)

a few minutes after the earthquake occurrence (Saito et al. 2011; Kubota et al. 2021). According to the example of SBPR-2 (Fig. 2), the response time of the internal temperature is supposed to be ~ 15 min in the observation system. Then, the difference between the internal temperature and the estimated temperature was hardly noticeable when the length of the time window is greater than ~ 10 days (Fig. 4b, c). After the initial rise of + 0.10 °C, the water temperature increased intermittently a few times (e.g., DOY 436, 438, and 440), but the amplitudes of the increases gradually decayed. On March 24, 2011 (DOY 447), we made TJT1 float up to the sea surface and successfully retrieved it. During both the falling and floating up of the equipment, there were temperature spikes that were lower than the temperature level when it was on the seafloor (Fig. 4b, c). This is because the adiabatic compression effect of seawater becomes noticeable
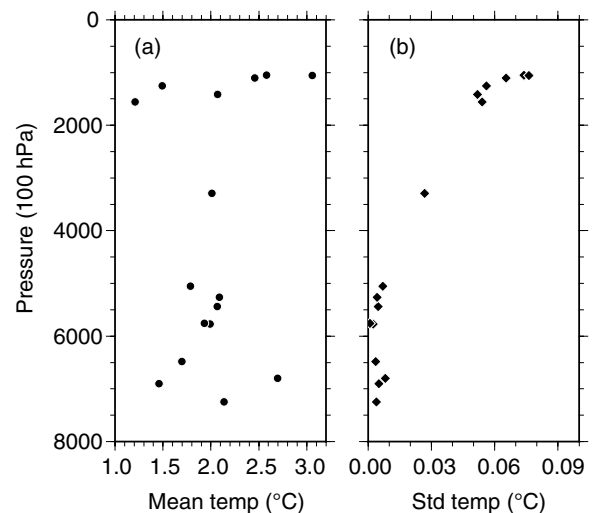
Fig. 5 **a** Mean and **b** standard deviation of the internal temperature records of 16 stations at offshore Tohoku (Fig. 1 and Table 1)

at sea depths greater than ~ 4 km, and there is a local minimum around the 4 km depth in the seawater temperature (e.g., Talley et al. 2011). As will be shown later, such temperature spikes were not visible at stations where the installed depths were shallower than ~ 4 km.

3.2 Temperature records of eight stations

Basic statistics of the seafloor water temperature derived from the built-in thermometers are compiled when there was no influence from the M_w 9 mainshock. Figure 5 shows the mean and standard deviation of the recorded temperature at respective depths for the eight stations that experienced the mainshock and the other eight stations after the earthquake (Fig. 1 and Table 1). The mean temperature ranged from 1.0 to 3.0 °C at seafloor depths of 1.1–7.3 km and showed no apparent dependence on the seafloor depth. The standard deviation was clearly smaller with greater depths. According to background oceanographic fields known by traditional hydrographic and modern Argo observations, the water temperature and its standard deviation both decrease with the sea depth (e.g., Gaillard et al. 2009; Tally et al. 2011). As mentioned in Sect. 2, although the absolute value of the internal temperature might not be so reliable with errors of ± 0.5 °C or more, the measured variations were mostly reliable at time scales greater than a few tens of minutes (Fig. 2). The feature that the standard deviation of the seafloor water temperature is smaller in deeper seafloors has been also confirmed by seafloor heat-flow observations (Yamano et al. 2014) and by temperature recordings of built-in thermometers of seafloor pressure gauges of the JAMSTEC's cable system (Gomberg et al. 2021).

Figure 6 shows all the temperature records of the eight stations from deployments to recoveries of the respective instruments. The recoveries of the seafloor instruments were carefully carried out since we expected that there might be movement, tumbling, and burial of the instruments due to landslide and sediment redeposition possibly induced by the mainshock. For TJT1, TJT1-2, P06, and P02, we made them float up from the seafloor by an ordinary acoustic release of the anchor and successfully recovered them. For GJT3, we carried out several trials of the acoustic release but failed and abandoned it on May 25 (DOY 509). The equipment GJT3 was somehow released from the anchor, floated up on May 31 (DOY 515), and drifted at the sea surface for several days, which was deduced from the pressure/temperature records. The JAMSTEC's R/V *Natsushima* incidentally found the drifting GJT3 and kindly picked it up. Using a remotely operated vehicle to go to the
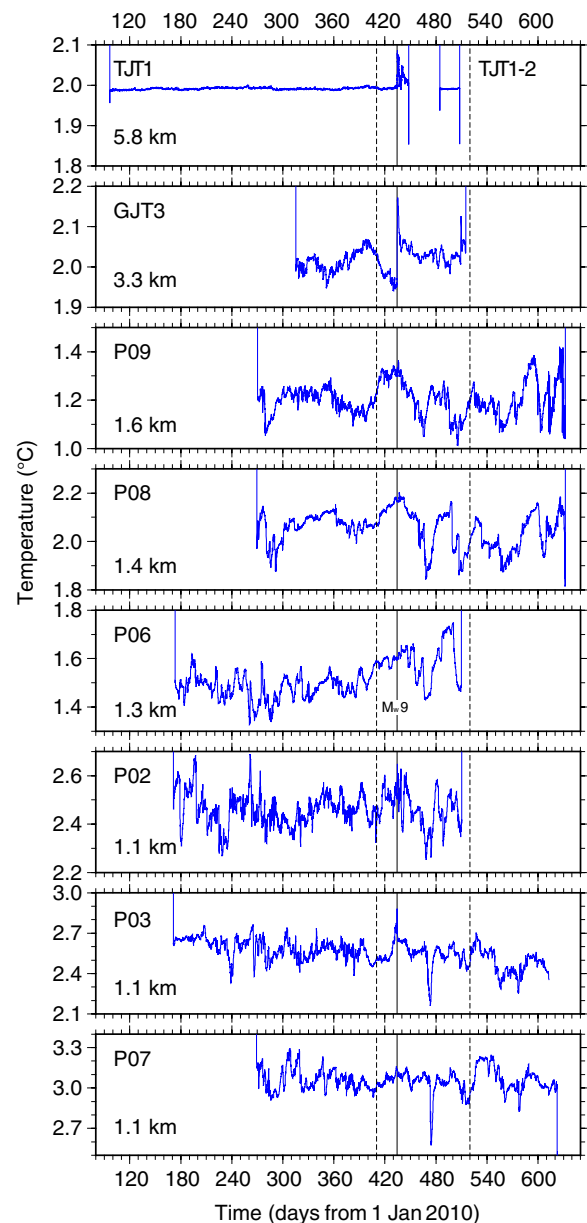
Fig. 6 Time series of the internal temperature of 8 stations during DOY 90–660. The top panel also includes TJT1-2 during an observation period from April 30 to May 24, 2011. The temperature of TJT1-2 is shifted by + 0.06 °C to meet the background temperature level of TJT1. The M_w 9 mainshock occurrence is indicated by solid vertical lines at DOY 434.2403. Time windows between the dashed lines indicate those shown in the next figure (i.e., Fig. 7)

seafloor, we directly salvaged P09, P08, P03, and P07 (Hino et al. 2012; Arai et al. 2013; Kawamura et al. 2021).

The observed temperature at the seafloor is described (Fig. 6). No significant instrumental drift was found in all the temperature records. Noticeable correlations of temperature variations were found between P08 and
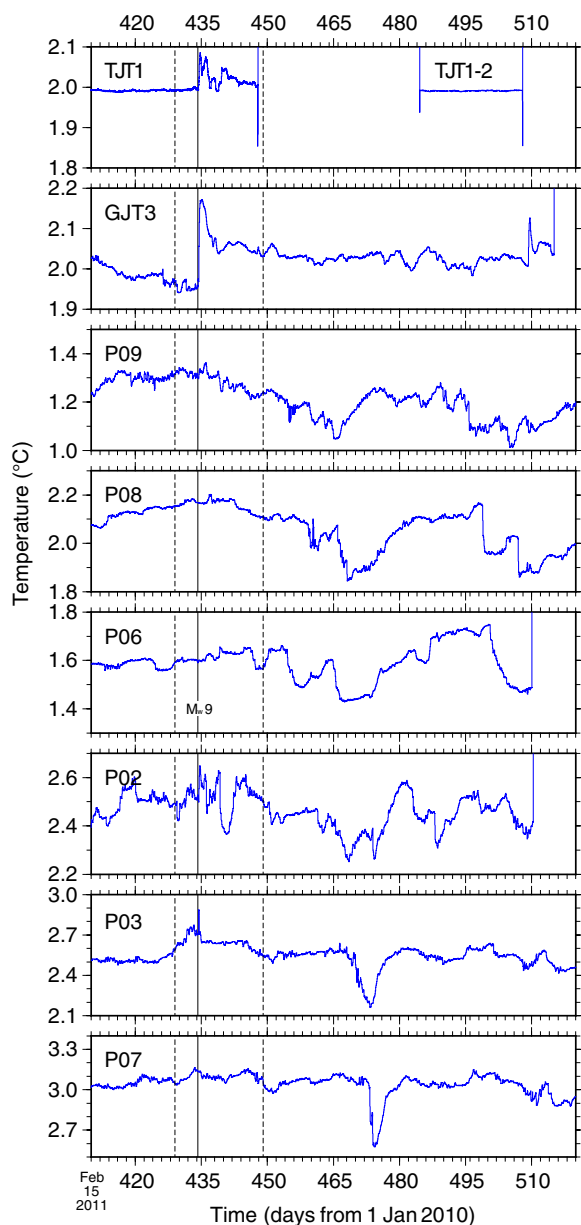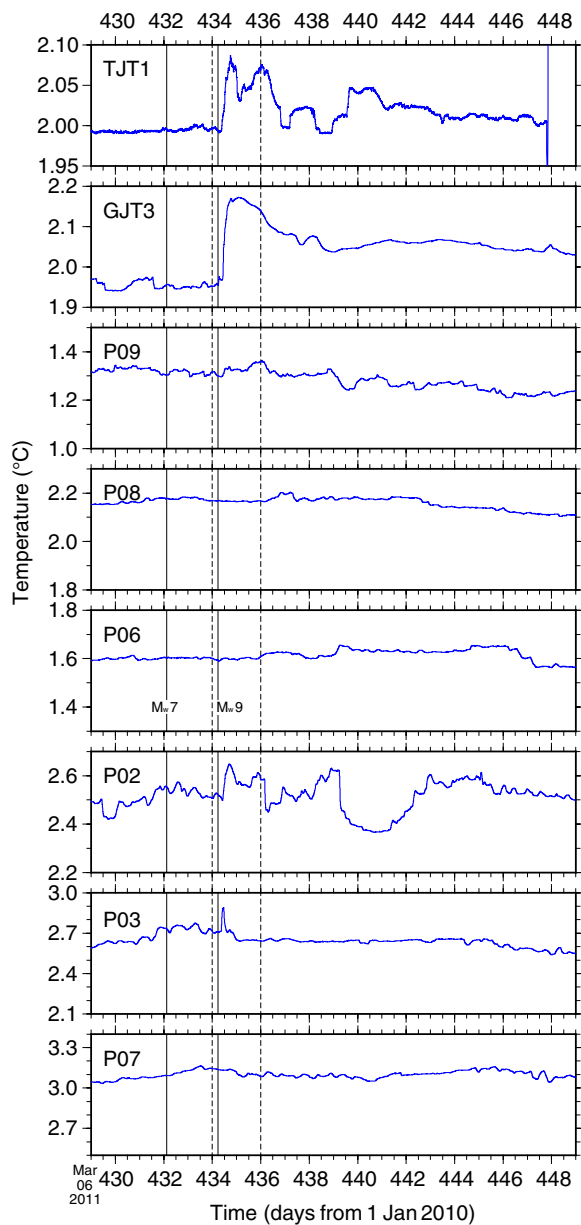
Fig. 7 Same as Fig. 6 but for DOY 410–520

P09, between P02 and P06, and between P03 and P07 (Figs. 6 and 7). Horizontal distances between these pairs were almost 20–30 km (Fig. 1). Such correlations with comparable distances were also found by the built-in thermometer records of the JAMSTEC's cable system (Gomberg et al. 2021). Correlation distances related to the seafloor temperature variations were considerably shorter than those found in low-frequency (e.g., < 0.5 cycles per day) seafloor pressure variations which showed clear similarities over spatial scales of ∼ 100 km (e.g., Donohue et al. 2010; Dobashi and Inazu 2021;

Inoue et al. 2021). The seafloor temperature at offshore Tohoku is likely affected by ocean currents such as Oyashio/Kuroshio with mesoscale eddies, but the relationship between those ocean currents and deep-sea (depths > ∼ 1 km) water temperature has not been so clarified (e.g., Kakehi et al. 2021).

We see the temperature variations before and after the mainshock (Figs. 7 and 8). Two days before the mainshock, the M_w 7 foreshock occurred just below the observation sites (DOY 432.1146 or 02:45 UT on March 9, 2011). The seismic vibration, crustal deformation, and tsunami were evident in the seafloor pressure records just after the foreshock occurrence (Hino et al. 2013; Kubota et al. 2017). Meanwhile, all the stations showed no clear temperature anomaly related to the foreshock (Fig. 8). No anomalous temperature change was also found within minutes after the mainshock occurrence (Figs. 8 and 9) although the seismic vibration, crustal deformation, and tsunami were extremely evident in all the pressure records during this period (Kubota et al. 2021).
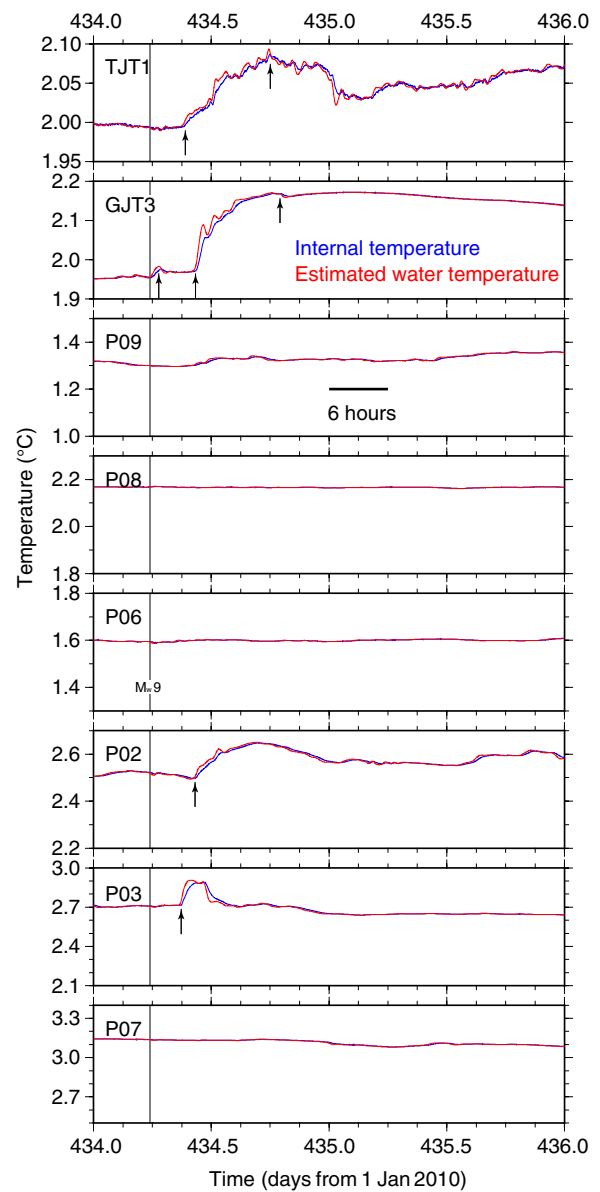
Significant temperature anomalies occurred several hours after the mainshock (Fig. 9). At TJT1, the temperature began to rise 3.5 h after the mainshock, took another 9.0 h to reach a peak of + 0.10 °C, and roughly decayed until the equipment was retrieved on March 24, 2011 (Fig. 8). The temperature decay was composed of several intermittent rises with decreasing their peak amplitudes. The intermittent rises are hereafter called "subevents." They were evident for + 0.08 °C during DOY 435–436 (March 12), + 0.03 °C during DOY 437 − 438 (March 14), and + 0.05 °C including a slight change of + 0.02 °C during DOY 439–440 (March 16). Another observation of TJT1-2 from April 30 to May 24 showed that the temperature fluctuations were as small as those of TJT1 before the M_w 9 mainshock (Figs. 6 and 7), which indicated that effects from the M_w 9 mainshock and aftershocks were fully gone ∼ 50 days after the mainshock occurrence. Thus, we infer that the temperature anomaly of + 0.10 °C almost decayed to the original level by ∼ 30 days after the mainshock (e.g., DOY 465).

At GJT3, there might be a slight temperature change of + 0.03 °C which occurred 1.2 h after the mainshock; however, this was hardly a significant anomaly since the slight change did not far exceed one standard deviation (i.e., 0.03 °C) at this station (Figs. 5, 8, and 9). The temperature began to rise 4.5 h after the mainshock and took another 9.0 h to reach a peak of + 0.20 °C (Fig. 9). The positive temperature anomaly smoothly decayed to the original level over ∼ 30 days (Figs. 6 and 7), which was comparable to the inferred time scale of the decay of the temperature anomaly of TJT1 (Figs. 7 and 8). A notable temperature spike of GJT3 found on DOY 509 (May 25) was probably due to an

Inazu *et al. Progress in Earth and Planetary Science* (2023) 10:24

Page 11 of 27

Fig. 8 Same as Fig. 6 but for DOY 429–449. The other solid vertical lines at DOY 432.1146 indicate the M_w 7 foreshock occurrence

Fig. 9 Time series of (blue) the internal temperature and (red) the estimated water temperature of 8 stations during DOY 434–436 (March 11–13, 2011). Arrows indicate possible onset or peak of temperature anomalies

artificial disturbance (Fig. 7) as mentioned above. Compared to TJT1, the decay process of GJT3 was relatively smooth without significant intermittent temperature rises (Figs. 7 and 8). Using the ambient temperature estimation from the built-in thermometer records, some temperature disturbances with a time scale of ~1 h appeared during the longer (i.e., ~9 h) increasing process in GJT3 (Fig. 9). Note that the onset time of the evident temperature anomaly was ~1 h earlier at TJT1 than at GJT3 (Fig. 9).

At P03, the temperature began to rise 3.1 h after the mainshock and took another 0.8 h to reach a peak of +0.19 °C. This temperature anomaly lasted for ~2 h and took another ~2 h to mostly return to the original temperature level (Fig. 9). Arai et al. (2013) investigated the temperature anomaly of P03 and suggested that the temperature anomaly was caused by a tsunami-generated turbidity current. During the temperature increase, the turbidity current displaced the equipment to a place that was 15 m deeper and ~1 km eastward from

the original position (Arai et al. 2013; Kawamura et al. 2021). The estimated ambient temperature showed that the onset and termination of the temperature anomaly of P03 was probably a sharp, box-shaped temperature change, compared to that shown by the original internal temperature record (Fig. 9).

At P02, the temperature might have begun to rise ~ 4 h after the earthquake (Fig. 9), but this was not likely a significant anomaly according to the background fluctuation level (Fig. 6). At the other four stations (P09, P08, P06, and P07) as well as P02, there were no notable temperature anomalies due to the mainshock (Fig. 9).

3.3 Temperature anomaly and pressure variations at TJT1 and GJT3

The seafloor temperature anomalies of TJT1 and GJT3 almost showed common features from their onsets to decays (Fig. 8). In this subsection, the temperature variations are compared to the pressure variations to examine possible explanations of the temperature anomalies.

The pressure variations are divided into two properties (Fig. 10). One is a dynamic pressure variation or vibration. The pressure vibration is recognized as a proxy of elastic/seismic waves (e.g., Nosov and Kolesov 2007; Saito et al. 2019). When we took a 1-h window to calculate the root-mean-square amplitude from the observed pressure records, robust pressure vibrations were commonly obtained at both TJT1 and GJT3 (Fig. 10a). The robust pressure vibrations involved the elastic/seismic waves and certain amounts from the tsunami (e.g., Saito et al. 2013; Kubota et al. 2021).

Another is a static pressure variation in which high-frequency (e.g., > ~ 1 cycle per minute) components are removed from the observed pressure records. The static variation is further divided into two parts: tidal and seafloor deformation components. Ocean tidal loading change has often affected undersea tectonic processes (e.g., Ide and Tanaka 2014; Römer et al. 2016; Wilcock et al. 2016). The seafloor deformation due to slow slips and postseismic slips has been identified in the residual pressure variation (e.g., Inazu et al. 2012; Ito et al. 2013; Fukao et al. 2021). We obtained the residual pressure (Fig. 10b) when tidal components, low-frequency oceanic variations predicted by numerical ocean modeling, and fitted instrumental drifts were properly removed from the static pressure variation (Inazu et al. 2012; Hino et al. 2014; Fujimoto et al. 2014).
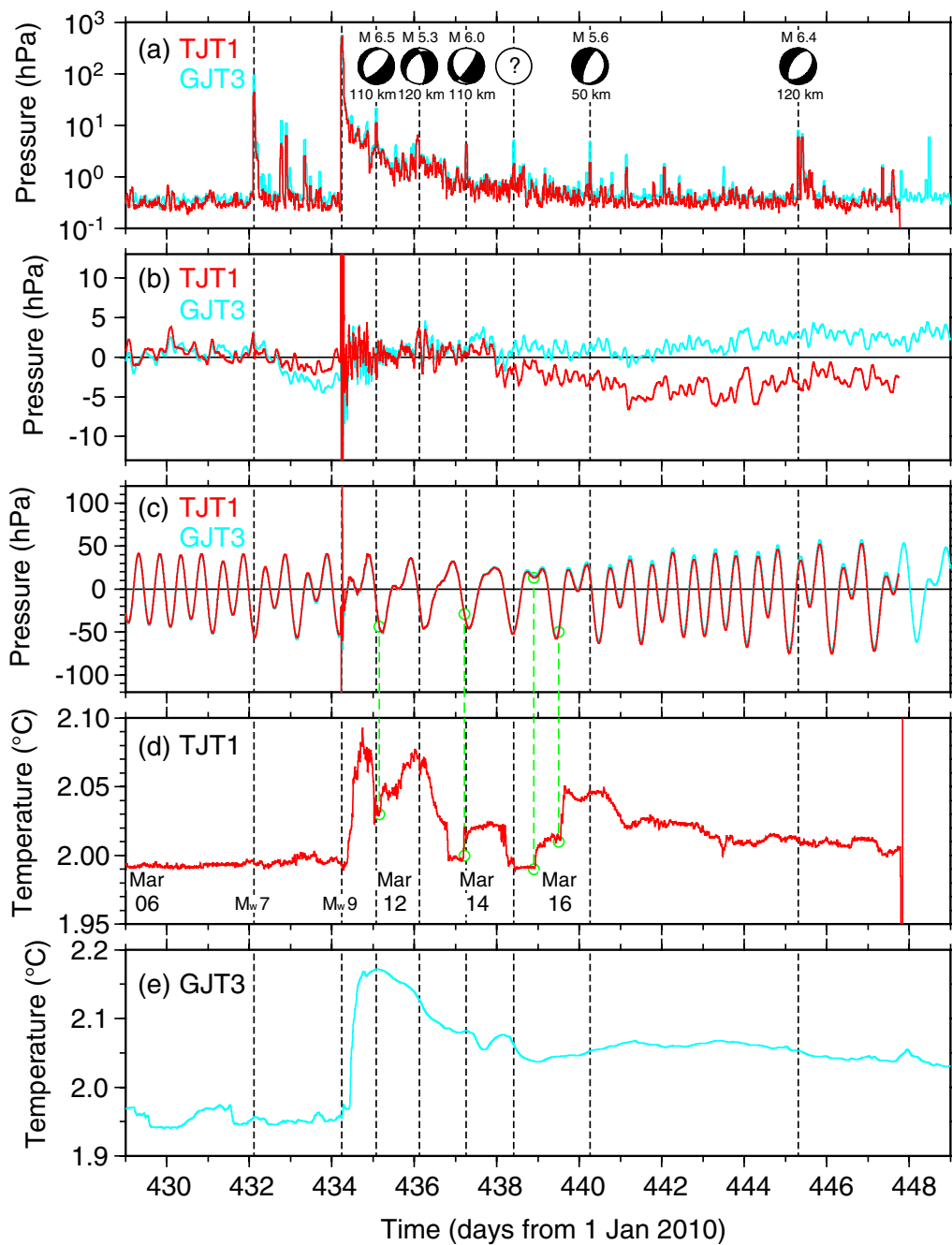
The pressure vibrations at TJT1 and GJT3 commonly decayed after the mainshock but exceeded unusually high levels over ~ 10 days (Fig. 10a). The decay of the pressure vibrations was substantially attributed to that of the tsunami (Tang et al. 2012; Saito et al. 2013; Fine et al. 2013). These decay time scales of the pressure vibrations were clearly shorter than those of the seafloor temperature anomalies (Fig. 10d and e). This indicates no relationship between the decay of the pressure vibrations and that of the temperature anomalies at TJT1/GJT3.

Many aftershocks occurred after the mainshock (e.g., Asano et al. 2011). Several distinct pressure spikes were induced by large (M_w 5–6) aftershocks which occurred within ~ 100 km from TJT1 or GJT3. Most of them were strike-slip and normal-fault earthquakes (Fig. 10a) based on the Global Centroid Moment Tensor catalog (Ekström et al. 2012). The temperature anomaly of GJT3 showed a relatively smooth decay and hardly showed a significant relationship with the pressure spikes due to the large aftershocks (Fig. 10a and e). When we compared the subevents of TJT1 to the pressure spikes (Fig. 10a and d), the onsets of the subevents sometimes began before the pressure spikes (i.e., DOY 435 and 437) or seemed to occur independently of the pressure spikes (i.e., DOY 436, 438, and 440). This indicates that there was no clear causal relationship between the subevents and nearby aftershocks. After DOY 441 (March 18), the temperature anomaly of TJT1 simply decayed without effects from nearby aftershocks or pressure vibrations (Fig. 10a and d).

Apart from large stepwise pressure changes due to the mainshock, the residual pressure variations showed post-mainshock seafloor deformation in the vertical direction (e.g., Inazu et al. 2012; Fujimoto et al. 2014). During 2 weeks after the mainshock, the residual pressure variation of GJT3 hardly indicated a notable slow seafloor vertical displacement which was less than ~ 5 cm (i.e., < ~ 5 hPa), and that of TJT1 indicated a transient, small seafloor elevation of ~ 5 cm (i.e., depression of ~ 5 hPa) during DOY 437–442 (Fig. 10b). Meanwhile, the other six observation sites (P02, P03, P06, P07, P08, and P09) showed typical afterslip changes of relatively large subsidence exceeding 10 cm during the 2 weeks (Fig. 5 of Fujimoto et al. 2014). The slow vertical displacements at TJT1 and GJT3 were relatively small compared to those at the other landward stations. The temperature decays of TJT1/GJT3 and the subevents of TJT1 hardly showed reasonable relationships with the small seafloor vertical displacements there.

The tidal loading change is examined for the subevents of TJT1. The subevents mostly seemed to occur during low or falling tides (i.e., DOY 435, 437, 438, and 439). Compared to the other examinations with the dynamic/static pressure variations, there was a possible relationship between the onsets of the subevents and the low-tide loading although the correlation between them may not be significant (Fig. 10c and d).

Fig. 10 Temperature records and pressure variations during DOY 429–449. **a**, **b**, and **c** denote dynamic pressure vibration, residual pressure, and tidal loading pressure (see texts in Sect. 3.3), respectively, at TJT1 and GJT3. In **a**, the dynamic pressure vibration amplitudes are calculated as root-mean-square amplitudes in respective 1-h time windows. Times of several distinct pressure spikes are marked by vertical dashed lines which are also attached to the other panels. Centroid-moment-tensor solutions of several aftershocks corresponding to the pressure spikes are attached. No reasonable solution is found corresponding to a pressure spike on DOY 438. The moment magnitude, mechanism, and distance from TJT1 are shown. Those parameters are based on the Global Centroid Moment Tensor catalog (Ekström et al. 2012). Large static pressure steps due to the M_w 9 mainshock in **b** and **c** are shifted to see small pressure changes before and after the mainshock in the same frames. **d** and **e** denote the estimated water temperature of TJT1 and GJT3, respectively. The onsets of the subevents of TJT1 and corresponding tidal loading levels are plotted by green circles and lines in **d** and **c**, respectively
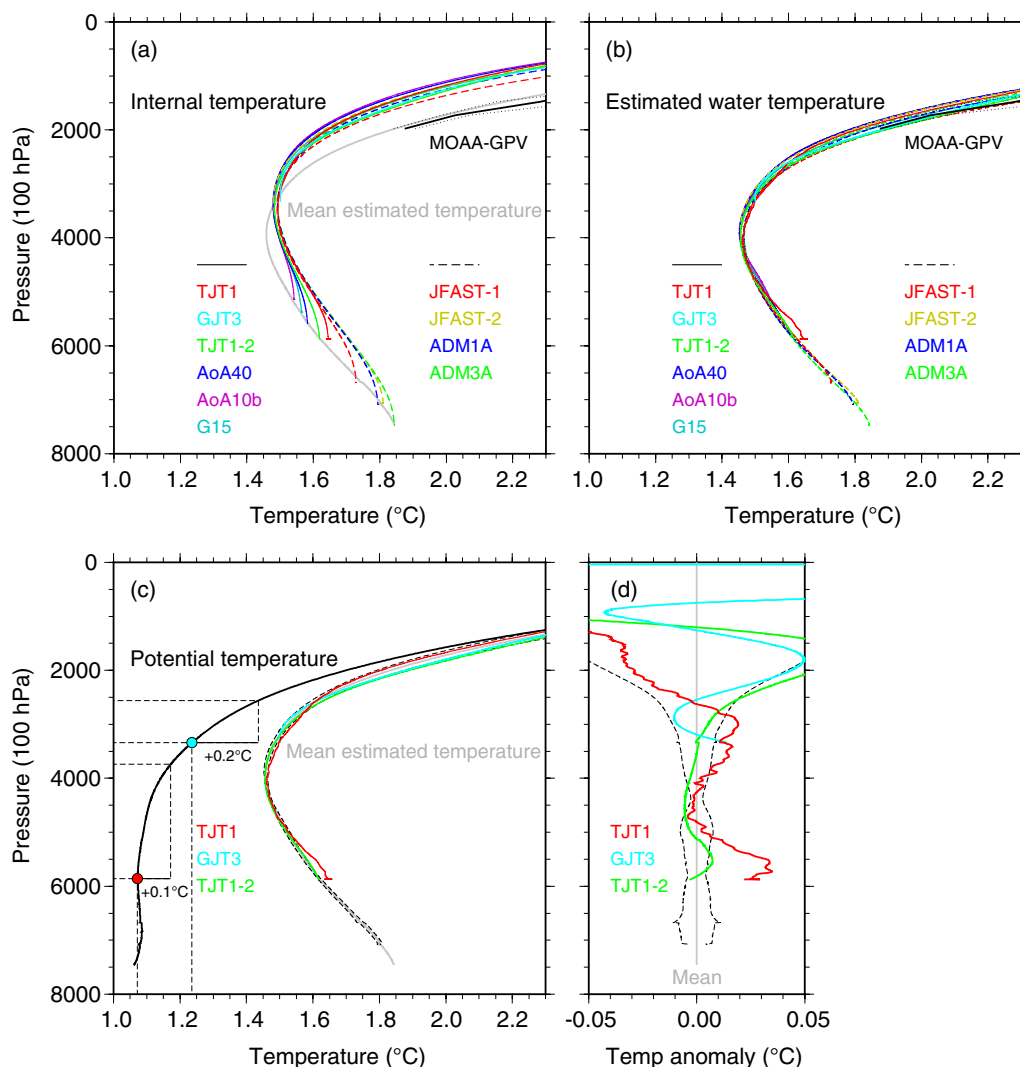
Fig. 11 Vertical profiles of **a** internal temperature, **b** estimated water temperature, **c** potential temperature calculated from mean estimated water temperature, and **d** temperature anomalies of TJT1, GJT3, and TJT1-2 from the mean profile. See Table 1 and Fig. 1 for the details of the stations. In **a** and **b**, solid curves include 6 stations at sea depths of 3.3–5.8 km, and dashed curves include 4 stations at sea depths of 6.5–7.2 km. The absolute values of the internal and estimated temperature are ad hoc shifted (e.g., shift range from −0.87 to +0.34 ℃) so that the vertical distributions are roughly consistent. A mean water temperature profile derived from MOAA-GPV at 38.5°N/143.5°E (black curve) is drawn with one standard-deviation interval (dotted curves). Gray curves in **a** and **c** indicate the mean estimated temperature profile which is calculated from the 7 profiles shown in **b** except for TJT1, GJT3, and TJT1-2. The potential temperature is calculated from the mean profile assuming a constant salinity of 34.5 PSU. One standard-deviation interval is attached with dashed curves to the mean profile in **c** and **d**. Effective ranges of +0.1 ℃ and +0.2 ℃ around TJT1 and GJT3, respectively, are attached to the potential temperature with dashed and thin lines in **c**

3.4 Vertical distributions of water temperature

Regarding the temperature anomalies found in TJT1 and GJT3 (Figs. 7, 8, 9, 10), we attempt to investigate the upper extensions of the seafloor temperature anomalies using the vertical distribution of water temperature during the floating up of these instruments. The vertical distributions of the internal temperature during the floating up are shown in Fig. 11a. In addition to TJT1 and GJT3, we plot deeper seafloor (depths of 5.1–7.3 km)

observations conducted after the mainshock (Fig. 1 and Table 1). Since the absolute values of the internal temperature may not be reliable (Fig. 5a), the absolute values of the temperature are ad hoc shifted so that the vertical distributions are roughly consistent at sea depths of 3–5 km including the temperature minimum layer. Water temperature changes are almost smaller in deeper seas (Fig. 5b), and we suppose that the minimum water temperature and associated zero vertical gradient at each

station can be used as a reference to be suitably consistent (Fig. 11a). A mean water temperature distribution shallower than 2 km depths at 38.5° N/143.5° E derived from Argo reanalysis data, MOAA-GPV (Hosoda et al. 2008), is also plotted for comparison.

Figure 11b shows the vertical distributions of the water temperature estimated from the internal temperature using Eq. (1). The floating speeds of the instruments were 0.8–1.2 m/s, as mentioned in Sect. 2. When we suppose a 15-min delay of the internal temperature, the vertical shift of the temperature profile is roughly expected to be up to ~ 1 km. Although the vertical structures of the internal temperature were apparently different between the stations near respective seafloors (Fig. 11a), those of the estimated water temperature almost showed identical from the respective seafloors to shallow depths (Fig. 11b). Thus, the estimated temperature reasonably captured that there were smaller water variations in deeper seas (e.g., Gaillard et al. 2009; Talley et al. 2011).

The estimated temperature could also trace the Argo reanalysis profile at sea depths shallower than 2 km (Fig. 11b). Figure 11c shows the water temperature profile averaged between the seven stations except for TJT1, TJT1-2, and GJT3. Figure 11d shows vertical distributions of the estimated temperature anomalies from the mean profile for TJT1, TJT1-2, and GJT3. A remarkable anomaly within + 0.03 °C that clearly exceeded one standard deviation was found up to ~ 500 m above the seafloor when TJT1 was floating up on March 24, which was achieved successfully by the estimated water temperature (Fig. 11b–d), not by the internal temperature (Fig. 11a). There was no such evident anomaly above TJT1-2 on May 24 and above GJT3 on May 31.

We calculate a potential temperature distribution (Bryden 1973; Gill 1982) from the mean profile to compensate for an adiabatic compression effect in deep seas (Fig. 11c). Since we focused on the deep seas (> ~ 2 km depths) and had no salinity information for the seafloor pressure observations, a constant salinity of 34.5 PSU was simply supposed based on the World Ocean Atlas 2018 (Zweng et al. 2019). Unlike the ambient water temperature, the potential temperature basically decreased with depth. The change rate of the potential temperature along the sea depth also decreased with depth, showing a typical, stable stratification (e.g., Talley et al. 2011). According to Fig. 11c, when we put water mass whose temperature is 0.1 °C (0.2 °C) greater than the surrounding seawater at a sea depth of 5.8 km (3.3 km) for TJT1 (GJT3), the warm water mass can likely move upward to ~ 2 km (~ 1 km) or sea depth of ~ 3.7 km (~ 2.5 km) as an upper limit constrained by neutral buoyancy.

3.5 Summary of the observed water temperature anomaly
The observed water temperature anomalies at the eight stations are summarized below.

TJT1: The seafloor water temperature began to rise 3.5 h after the mainshock, peaked at + 0.10 °C for another 9.0 h (Fig. 9), and decayed with intermittent rises (i.e., subevents). The subevents were evident for + 0.08 °C on March 12, + 0.03 °C on March 14, and + 0.05 °C on March 16 (Fig. 8). The onsets of the subevents seemed to occur during low or falling tides and hardly showed relationships with effects from the nearby distinct aftershocks or the post-mainshock vertical displacements there (Fig. 10). A water temperature anomaly of less than + 0.03 °C was found up to ~ 500 m above the seafloor during the floating up of the equipment 13 days after the mainshock (Fig. 11d). No temperature anomaly was found during the observation period from April 30 to May 24 (TJT1-2). Although there was no temperature observation between March 24 and April 30, it was likely that the temperature anomaly including the subevents almost decayed over ~ 30 days after the mainshock.

GJT3: The seafloor water temperature began to rise 4.5 h after the mainshock and peaked at + 0.20 °C for another 9.0 h (Fig. 9). The temperature anomaly smoothly decayed to its original level over ~ 30 days after the mainshock. The smooth decay hardly showed a relationship with the dynamic/static seafloor pressure vibrations (Fig. 10). No significant temperature anomaly was found above the seafloor during the floating up of the equipment on May 31 (Fig. 11d).

P03: The seafloor water temperature began to rise 3.1 h after the mainshock and peaked at + 0.19 °C for another 0.8 h. The temperature anomaly lasted for ~ 2 h and terminated within a few hours (Fig. 9). The equipment was moved to a deeper place during the temperature anomaly (Arai et al. 2013).

No significant water temperature anomaly related to the mainshock was detected at the other five stations (P02, P06, P07, P08, and P09) at seafloor depths of 1.1–1.6 km (Fig. 9). No water temperature anomaly related to the M_w 7 foreshock was detected at all the eight stations (Fig. 8).

4 Discussion
4.1 Possible processes to cause water temperature anomaly
The water temperature anomalies related to the mainshock were observed at TJT1, GJT3, and P03. The temperature anomalies were all increases. There are two possible processes to cause the water temperature to increase near the seafloor. One is that relatively warmer seawater at a shallower depth is brought to a deeper seafloor. When a turbidity flow involves higher density with

suspended sediments but warmer temperature than those of deeper region water, the penetration of the turbidity flow into the deeper region enables the seafloor water temperature to increase there. Another is that warm water related to a geothermal gradient (e.g., ~ 0.03 ℃/m) is emitted from the subseafloor. When subseafloor warm or hot water emerges on the seafloor more quickly than a subseafloor heat diffusion process, the seafloor temperature can locally increase. We discuss how these two different processes contributed to the observed seafloor water temperature anomalies.

4.2 Turbidity currents due to tsunami or landslide

In this subsection, we evaluate whether turbidity currents due to tsunamis or landslides could cause the temperature anomalies found at P03, GJT3, and TJT1.

Arai et al. (2013) explained that the water temperature anomaly of P03 was caused by a tsunami-generated turbidity current, which is reviewed here as well. The seafloor water temperature of P03 began to rise 3.1 h after the mainshock, peaked at + 0.19 ℃, and terminated within several hours (Fig. 9). We suppose a following process that the tsunami-generated turbidity current caused the temperature anomaly. The great tsunami generated immediately by the elastic seafloor deformation took ~ 0.5 h to reach a shallow sea of a depth of ~ 100 m and probably induced substantial amounts of sediment suspension by a tsunami current of 10^{-1} m/s (e.g., Sugawara and Goto 2012; Arai et al. 2013; Inazu et al. 2018), which likely caused the onset of the turbidity current. When we assume that this sediment-gravity flow took another ~ 2.6 h to reach P03 which was located ~ 50 km distant from the 100-m sea depth, the average speed of the sediment-gravity flow was ~ 5 m/s which was a possible speed to lift and displace the anchored P03 (e.g., Arai et al. 2013; Paull et al. 2018). The duration of the temperature anomaly of several hours was comparable to those caused by possible turbidity currents due to earthquakes and other sources found at depths of 1.0–2.5 km (e.g., Mikada et al. 2006; Talling et al. 2013; Xu et al. 2014). The above discussion on the onset time, amplitude, and duration of the seafloor temperature anomaly indicates that the temperature anomaly of P03 was caused by the tsunami-generated turbidity current, as was suggested by Arai et al. (2013).

We attempt to investigate the cause of the temperature anomalies of GJT3 and TJT1, respectively, especially for the initial temperature rises of + 0.20 ℃ of GJT3 and + 0.10 ℃ of TJT1 (Fig. 9). We speculate how far the turbidity current to displace P03 went powerfully downstream. If we assumed that the temperature increase in GJT3 was caused by the tsunami-generated turbidity current, the turbidity current that passed through P03 with ~ 5 m/s should have accelerated into a deeper seafloor to ~ 20 m/s ($= \frac{100\ \text{km}}{4.5-3.1\ \text{hours}}$) since the distance between P03 and GJT3 was ~ 100 km, and the temperature anomalies of GJT3 and P03 began to occur 4.5 and 3.1 h, respectively, after the mainshock. The turbidity current of 20 m/s might be possible as a maximum value but probably be suspicious as a mean speed (e.g., Hampton et al. 1996; Talling et al. 2013; Clare et al. 2020). Furthermore, if it had reached GJT3 with such a speed, the anchored equipment would have been likely swept away more than P03. There was no indication that GJT3 was swept away as deduced from its pressure data. Hence, it was not evident that the tsunami-generated turbidity current strongly affected GJT3.

The turbidity current maintains high-speed propagation due to its higher density than the surrounding water. The high density is kept by replacing water and seafloor sediments at the propagation front. This is called an auto-suspension or self-accelerating mechanism (e.g., Parker et al. 1986; Sequeiros et al. 2018; Heerema et al. 2020). The amplitude of the water temperature anomaly of the turbidity current typically decreases with its intrusion into a deeper, cooler seafloor. For example, Hughes Clarke (2016) reported that positive temperature anomalies of 1.5–2.0 ℃ of turbidity-current sources have been often reduced to 0.1–0.3 ℃ after downward traveling of only 10^2 m at a shallow sea (depth of < 100 m). According to the data shown by Kakehi et al. (2021), the source temperature of the tsunami-generated turbidity current that caused the + 0.19 ℃ anomaly at P03 was deduced to be 5–8 ℃ at the 100-m sea depth in March 2011. The temperature anomaly at GJT3 was + 0.20 ℃, indicating no significant decrease in the temperature anomaly from P03 to GJT3. The above discussion on the expected propagation speed and the temperature anomaly decay of the tsunami-generated turbidity current suggests that a different major factor should be instead considered for the initial temperature anomaly of GJT3.

Since the initial temperature anomaly of TJT1 began ~ 1 h earlier than that of GJT3 (Fig. 9), the initial temperature anomaly of TJT1 was not attributed to that of GJT3. The TJT1 anomaly should have originated at a depth deeper than GJT3. Turbidity currents can be also induced by seafloor landslides which are often caused by strong seismic ground motion (e.g., Talling et al. 2007; Shanmugam 2015). If both distinct landslide and associated turbidity current had immediately occurred within 3.5 h after the mainshock on a slope between TJT1 and GJT3, the onset of the TJT1 anomaly might have been possibly explained. However, if the temperature increase of + 0.10 ℃ at TJT1 had been caused by such a landslide-generated turbidity current, the turbidity

Inazu *et al. Progress in Earth and Planetary Science* (2023) 10:24

Page 17 of 27

current should have occurred at a depth shallower than ~ 3.7 km as constrained by the potential temperature structure considering the TJT1 anomaly (Fig. 11c), and at a depth deeper than GJT3 (sea depth of 3.3 km) according to the earlier onset of TJT1. The warmth of the turbidity-current source is quickly lost with its intrusion into a deeper seafloor, as mentioned above. Since the potential water temperature at sea depths of 3.3–3.7 km was only 0.10–0.17 °C greater than that at TJT1 (Fig. 11c), this weak anomaly unlikely yielded the + 0.1 °C anomaly at TJT1 after downward traveling greater than ~ 10 km (Fig. 1). Hence, we suggest that warm water discharge from deep-sea subseafloor would be a promising process to cause the initial temperature anomaly of TJT1.

For the initial temperature anomaly of GJT3, we do not completely deny a possibility that landslide and associated turbidity current might have occurred at a depth shallower than GJT3 just after the mainshock and affected GJT3 alone. According to the constraint of the potential temperature structure (Fig. 11c), if a turbidity-current source induced by a landslide is considered to cause the GJT3 anomaly of + 0.20 °C, it requires that the source should have been located at sea depths at least shallower than ~ 2.5 km, and likely further requires that the source temperature anomaly should have been higher than, for instance, + 1 °C which indicates that the source should have been located at sea depths shallower than ~ 1.5 km. Such a shallow seafloor area was located ~ 50 km distant from GJT3 (Fig. 1). However, there were not likely landslides at the shallow, less steep slopes (~ 1°), than at deeper, steep slope regions (5 − 8°) near the trench (e.g., Kodaira et al. 2020). Indeed, there was no significant temperature anomaly at shallower places of P08 and P09. Furthermore, there was little evidence of long-distance (> ~ 10 km) lateral transports of suspended sediments except in the case of the tsunami-generated turbidity current which strongly affected P03 (Arai et al. 2013; Ikehara et al. 2021). Thus, turbidity currents which might be related to seafloor landslides were also less probable to cause the + 0.20 °C anomaly of GJT3. Warm water discharge from deep-sea subseafloor would be a promising process for GJT3 as well as the case of TJT1.

The water temperature anomalies of both TJT1 and GJT3 were roughly comparable in terms of the time scales of the initial rise and the decay. As shown in Figs. 7−9, those seafloor water temperature anomalies began to rise 3.5 or 4.5 h after the mainshock, both took ~ 9.0 h to reach respective peaks of + 0.10 °C or + 0.20 °C, and both decayed over ~ 30 days. These time scales were much longer than those observed at P03 (Fig. 9). It is reasonable to consider that the temperature anomalies of TJT1

and GJT3 from the initial rises to respective decays were caused by larger-scale phenomena than typical turbidity currents. We suppose that warm water discharges from the subseafloor would be suitable processes to dominantly cause the initial temperature rises of GJT3 and TJT1. We also note that the seafloor temperature anomalies of + 10^{-1} °C with durations of a few tens of days are comparable to those sometimes found in water temperature observations typically located kilometers from sources of hydrothermal event plumes (e.g., Lupton 1995; Murton and Redbourn 2000; Di Iorio et al. 2012), which suggests that a large-scale thermal phenomenon likely occurred although submarine volcanism is inactive at the landward slope of the Japan Trench.

The subevents found at TJT1 are also examined (Fig. 10). Since similar variations like the subevents were not evident at GJT3, the subevents probably originated nearer TJT1 or deeper places than GJT3. After the mainshock, landslides and associated turbidity currents might be easily induced by medium or large aftershocks. If we assumed this process, the subevents of TJT1 should have occurred after the distinct aftershocks. However, observed onset time differences between the subevents and the aftershocks did not suggest such a causal relationship (Fig. 10a and d). In addition, if the turbidity-current source was located at a place deeper than GJT3 and shallower than TJT1, the temperature anomaly of its source was at most + 0.2 °C compared to TJT1, according to the potential temperature structure (Fig. 11c). Such a small anomaly was unlikely to yield + 0.08 °C or + 0.05 °C at TJT1 after downward traveling of the turbidity current. Warm water discharges from the subseafloor should be reasonable processes to cause the TJT1 subevents as well as the initial temperature rise.

4.3 Warm water from subseafloor

We explain tectonic and oceanic features related to the warm water discharges and spreading which could cause the initial temperature anomalies of GJT3/TJT1 and the subevents of TJT1.

Geothermal structures below the seafloor around trench axes have been modeled (e.g., Gutscher and Peacock 2003; Saffer and Tobin 2011; Kimura et al. 2012). The Japan Trench Fast Drilling Project (JFAST) according to the Integrated Ocean Drilling Program (IODP) Expedition 343/343 T (Chester et al. 2013) carried out a direct measurement of temporal changes of the vertical structure of the subseafloor temperature in the frontal prism and confirmed a typical geothermal gradient of ~ 0.03 °C/m (e.g., Becker et al. 2020) even after the mainshock (Fulton et al. 2013, 2019). There was suitably
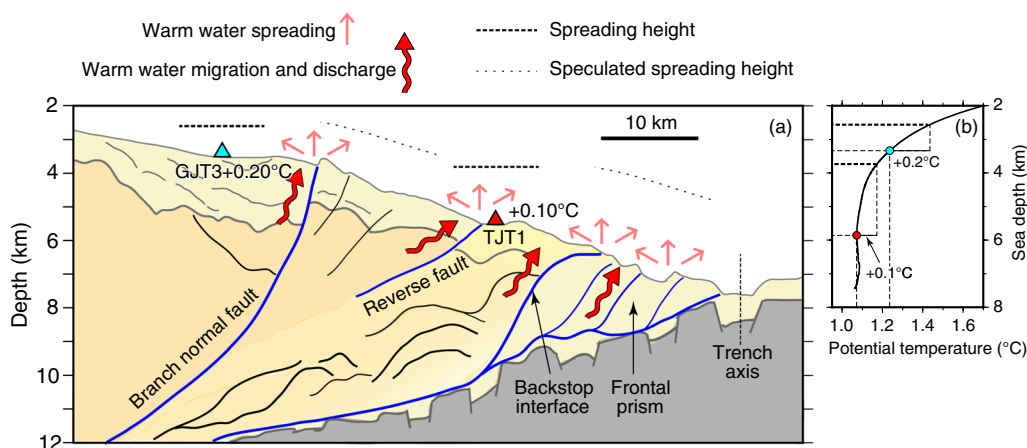
Fig. 12 Schematic illustration of the scenario of the warm water discharges and spreading. **a** shows the warm water discharges via multiple faults and the spreading of the discharged water. The spreading height (bold dashed lines) is plotted based on **b** potential temperature structure which is taken from Fig. 11c

warm water below the seafloor around the Japan Trench (e.g., 10^1 °C at a few kilometers below the seafloor) both before and after the mainshock (Kimura et al. 2012). The seafloor temperature is likely to increase when the sub-seafloor water from certain depths is discharged.

There are possible migration pathways of subseafloor fluids around TJT1 and GJT3 (Fig. 1). Repeating seismic explorations along the MY102 section have revealed that there are seafloor outcrops of faults such as the branch normal fault between TJT1 and GJT3, the reverse fault near TJT1, the backstop interface, and several reverse faults in the frontal prism (e.g., Miura et al. 2005; Tsuji et al. 2013; Kodaira et al. 2020). These seafloor fault outcrops are mostly shown as linear traces that are subparallel with isobaths and/or the trench axis. Tsuji et al. (2011) found chemosynthetic communities (e.g., *Calyptogena* colonies) at an outcrop of the reverse fault near TJT1 before the mainshock, which indicated that the reverse fault had worked as a stable fluid pathway to provide cold seeps to feed the communities. Similar chemosynthetic communities with possible cold seeps were also found at the frontal prism at the northern Japan Trench around ~40°N (Ogawa et al. 1996; Fujikura et al. 1999, 2002). We infer that there were also comparable fluid pathways with seafloor outcrops at the frontal prism in the vicinity of the MY102 section. Once those faults were severely ruptured by the mainshock slip, the warm fluids (e.g., 10^1 °C) became able to effectively migrate via those faults and emerge at the seafloor.

The discharged warm water at the seafloor can spread horizontally due to the eddy (i.e., turbulent) diffusion, and vertically due to the buoyancy. When we suppose typical horizontal eddy diffusivity coefficients (10^{-1}–10^0

m²/s), a turbulent diffusion speed of the water temperature anomaly (i.e., effective thermal diffusion) is 10^{-2}–10^{-1} m/s for several hours (e.g., Bemis et al. 1993; Lavelle and Baker 1994; Lavelle 1995). This indicates that the discharged warm water likely spreads out several kilometers over several hours. In the vertical direction, the relatively warm water spreads up to the height of neutral buoyancy which depends on the anomaly from the potential water temperature structure (Fig. 11c). When the temperature anomaly of the discharged water is $+10^0$ °C near the seafloor outcrop, vertical spreading speed of the warm water may be up to 10^{-1} m/s above the outcrop for hydrothermal event plumes (e.g., Lavelle and Baker 1994; Lavelle 1995).

4.4 Scenario of warm water discharge from subseafloor

We propose a scenario to reasonably explain the temperature anomalies of GJT3 and TJT1 based on the possible processes of the warm water ejections via subseafloor pathways and the spreading of the discharged water near the seafloor. Figure 12 shows the illustration of the scenario. The details of the observed features to be explained were described in Sect. 3.5.

The M_w 7 foreshock occurrence generated no effective pathway of subseafloor warm water to the seafloor. Strong ground shaking due to the foreshock might have made seafloor sediments suspended but associated water mixing could not cause the seafloor temperature anomaly (Fig. 8).

The M_w 9 mainshock occurrence induced larger slips closer to the trench axis (e.g., Iinuma et al. 2012). These slips involved anelastic deformation which probably

generated effective pathways of subseafloor warm water. The generated pathways were mainly composed of the branch normal fault between GJT3 and TJT1, the reverse fault near TJT1, the backstop interface, and perhaps reverse faults at the frontal prism (Kodaira et al. 2012, 2020; Tsuji et al. 2013).

Although we could not determine the exact time of the water discharge from the seafloor, the warm water was ejected via at least two pathways among those faults within a few hours after the mainshock. One of the pathways was the branch normal fault whose seafloor outcrop was located between GJT3 and TJT1. The other was the reverse fault near TJT1 or the backstop interface. Since the effective thermal diffusion speed was supposed to be 10^{-2}–10^{-1} m/s in the horizontal direction, the warm water ejected via the branch normal fault could spread over several kilometers and reach GJT3 for the next several hours. This warm water could not affect TJT1 which was located at a deeper place. The warm water ejected via the reverse fault near TJT1 and/or the backstop interface could, respectively, spread over several kilometers and reach TJT1. It is unclear which contribution was dominant. This warm water affecting TJT1 hardly affected GJT3 since the water temperature anomaly more diffused and decayed with longer-distance spreading (Fig. 12). As a result, the seafloor temperature of TJT1 and GJT3 began to rise 3.5 and 4.5 h, respectively, after the mainshock (Fig. 9).

When the water temperature anomaly became + 0.1 °C or + 0.2 °C after the horizontal spreading of kilometers from the seafloor outcrops, the temperature anomalies near the outcrops were likely greater than 10^0 °C (e.g., Lavelle 1995). The temperature anomaly of the subseafloor warm water source should be substantially higher than this 10^0 °C, for instance, 10^1 °C or more. The subseafloor warm water source with a temperature anomaly greater than 10^1 °C was supposed to be located deeper than a few kilometers below the seafloor, according to the geothermal gradient of 0.03 °C/m (Kimura et al. 2012; Fulton et al. 2013). Note that extremely high speeds of a few kilometers per a few hours (i.e., 10^{-1} m/s) of the subseafloor fluid advection via a few fault pathways were probably realized without submarine active volcanos there.

The warm water ejected via the branch normal fault contributed to the temperature anomaly of GJT3 alone, and smoothly decayed over ~ 30 days after the mainshock (Figs. 7, 8, and 10). The warm water discharges which contributed to the initial temperature anomalies of GJT3 and TJT1 occurred within a few hours after the mainshock. From several hours to several days after the mainshock, intermittent warm water ejections probably occurred via multiple fault pathways whose seafloor outcrops were located near or deeper than TJT1. Candidates of those fault pathways are the reverse fault near TJT1, the backstop interface, and perhaps the reverse faults at the frontal prism. They were severely ruptured due to the mainshock, and warm water likely migrated and approached close to the seafloor outcrops. Low and falling tidal loading possibly helped the subseafloor warm water close to the seafloor outcrops to intermittently emerge at the seafloor (Fig. 10). Some of the warm water discharges caused the subevents of TJT1 although it is unclear which fault pathways dominantly contributed to the respective subevents. The intermittent warm water discharges almost decayed over ~ 30 days after the mainshock.

The relatively warm water discharged from the subseafloor efficiently spread upward due to buoyancy. As mentioned in Sect. 3.4, according to the potential temperature structure with the seafloor temperature anomalies (Fig. 11c), the initial temperature anomalies at TJT1 and GJT3 likely spread vertically up to ~ 2 km and ~ 1 km above the seafloor, respectively, which means the warm water spreading up to the sea depths of ~ 3.7 km above TJT1 and ~ 2.5 km above GJT3, respectively (Fig. 12). Although the discharged water nearer the seafloor fault outcrops was probably warmer and spread above more, the actual spreading heights above the fault outcrops could not be well constrained. The vertical spreading of the warm water anomaly above TJT1 gradually decayed but remained within + 0.03 °C up to ~ 500 m above the seafloor 13 days after the mainshock. The expected warm water spreading above GJT3 also decayed. The water temperature anomalies at TJT1 and GJT3 both became undetectable ~ 30 days after the mainshock.

4.5 Consistency of the scenario with other studies

The proposed scenario of the warm water discharge is examined with other studies of geophysical, geochemical, and geological observations which were mostly carried out after the M_w 9 mainshock.

We supposed that the migration pathways of the warm water were the branch normal fault between GJT3 and TJT1, the reverse fault near TJT1, the backstop interface, and the several reverse faults at the frontal prism (Fig. 12). Tsuji et al. (2013) carried out heat-flow measurements at the epicentral region five and seventeen months after the mainshock and suggested that the branch normal fault worked as a bulk pathway of the leakage and decay of the geothermal heat. They also found seafloor fissures where anelastic deformation occurred related to a large extensional strain of > 10^{-3} between GJT3 and TJT1 (Ito et al. 2011; Sato et al. 2011; Kido et al. 2011) and perishing of chemosynthetic communities at the seafloor outcrops of the reverse fault

near TJT1 and of the backstop interface. These results indicated drastic subseafloor fluid discharge and its decay from these fault pathways months after the mainshock. Also, an extensional regime in the upper plate after the mainshock, which was suggested by studies of seismicity (e.g., Kato et al. 2011; Hasegawa et al. 2012) and those of borehole breakout (e.g., Lin et al. 2013; Brodsky et al. 2020), was possibly compatible with the effective subseafloor fluid migrations. Our seafloor temperature records suggested the abrupt heat discharges with their early decays via the branch normal fault and the multiple faults at deeper places during at least 2 weeks after the mainshock. These suggested processes will help to further discuss the subseafloor fluid/heat behaviors with the post-mainshock survey results.

The chemical anomalies of ^{13}C/^{12}C and ^{3}He/^{4}He near the epicentral seafloor were detected from the sampled water that was obtained 36 days after the mainshock (Kawagucci et al. 2012; Sano et al. 2014). The turbidity anomaly near the seafloor was also detected during the water sampling (Noguchi et al. 2012). Although those chemical and turbidity anomalies were detected, Kawagucci et al. (2012) noted no water temperature anomaly detected at sea depths up to ~ 5.7 km at that time. The observed seafloor temperature anomalies were almost undetectable ~ 30 days after the mainshock (Fig. 7), which was compatible with the note of Kawagucci et al. (2012). The decay time scale of the temperature anomaly was apparently shorter than that of the chemical and turbidity anomalies.

Our scenario is that the subseafloor warm water source whose temperature was likely greater than 10^1 °C at a place deeper than a few kilometers was discharged to the seafloor within a few hours after the mainshock. The discharged warm water involved subseafloor materials integrated along the fluid pathway from the warm water source to the seafloor. The seafloor sediment was suspended above due to the warm water discharge and spreading. Thus, the observed anomalies of ^{13}C/^{12}C (i.e., methane at 1–2 km below the seafloor) and of turbidity near the seafloor probably began to spread with the warm water discharge. We speculate when the ^{3}He/^{4}He anomaly was emitted. Sano et al. (2014) suggested that the mantle-derived ^{3}He/^{4}He anomaly was located at distances of 30–150 km from the epicentral seafloor before the mainshock. Park et al. (2021) found that fluids possibly involving ^{3}He/^{4}He anomalies characterized by strong seismic reflections were distributed on patches at shallow regions (2–10 km depth) along clear faults including the branch normal fault. We infer that some portions of the shallow fluids involving the ^{3}He/^{4}He anomalies were also discharged with the shallower methane quickly after the mainshock. It is unclear whether deeper (> 20 km

depth) fluids were discharged to the seafloor. Anyway, the deeper fluids probably migrated to shallower regions and were efficiently held there, which was seismically imaged by Park et al. (2021).

Since grain sizes of the seafloor sediments are ordinarily finer at far offshore, deeper seafloor, it takes much time to settle again once they are suspended. When we suppose that the seabed sediments mainly consist of silt whose typical diameters are ~ 10 μm at the landward slope of the Japan Trench at seafloor depths of 3–6 km, and employ a Stokes equation (Gibbs et al. 1971; Dietrich 1982), the settling velocity is 10^{-4} m/s for the silt (e.g., Noguchi et al. 2012). As mentioned in Sect. 4.3, vertical spreading speeds of the discharged warm water may be up to 10^{-1} m/s above the seafloor outcrops (Lavelle and Baker 1994; Lavelle 1995). The vertical spreading speeds of the discharged warm water were much faster than the settling velocity of suspended sediments in the deep sea. Also, fine or dissolved materials are prone to be captured by suspended sediments. Thus, the diffusion or decay of the water temperature anomaly was much faster than that of the turbidity and the chemical anomalies. The following processes are then reasonable: Both the temperature anomaly and the chemical/turbidity anomalies spread over 1 or 2 km above GJT3 or TJT1 due to the buoyancy (Fig. 12). The temperature anomalies decayed and became undetectable ~ 1 month after the mainshock (Fig. 7). The suspended sediments with the chemical anomalies slowly settled down. They efficiently remained up to ~ 1 km above the seafloor ~ 1 month after the mainshock (Noguchi et al. 2012; Kawagucci et al. 2012; Sano et al. 2014).

Noguchi et al. (2012) and Ikehara et al. (2021) explained that the turbidity anomalies with the suspended sediments were caused by strong ground motion, induced landslides, strong tsunami currents, and associated turbidity currents. After the mainshock, landslides and associated turbidity currents were prone to occur due to moderate and large aftershocks, especially at deeper, steeper slope regions near the Japan Trench (e.g., Ikehara et al. 2016; Kodaira et al. 2020; McHugh et al. 2020). They likely induced local water mixing with turbidity anomaly but unlikely caused detectable water temperature anomaly in the deep seas, as deduced from the potential temperature structure (Fig. 11c). Meanwhile, the warm water discharge probably dispersed the seafloor sediments laterally and upward around the outcrops of the subseafloor fluid pathways. This is suitably added as another factor to the causes of the turbidity anomalies explained by Noguchi et al. (2012) and Ikehara et al. (2021).

We have explained that the proposed scenario of the warm water discharges from the subseafloor was mostly compatible with geophysical (Tsuji et al. 2013; Park et al.

2021), geochemical (Kawagucci et al. 2012; Sano et al. 2014), and geological (Noguchi et al. 2012; Ikehara et al. 2021) observations which were carried out after the mainshock. It is plausible that the warm water discharges which occurred within a few hours after the mainshock simultaneously brought the spreading of the seafloor sediments with the methane/helium from at least a few kilometers below the seafloor.

4.6 Discharged heat during the mainshock

We discuss the heat properties of the initial temperature anomalies of GJT3/TJT1. Based on the extent of the warm water spreading around GJT3 and TJT1 (Fig. 12), the heat content and flux of the discharged water are roughly estimated. The discharged warm water almost extended a few tens of kilometers in the east–west direction ($D_{EW} = 3 \times 10^4$ m) and hundreds of meters above the seafloor ($h_w = 10^2$ m). We assume that the extension was also a few tens of kilometers in the north–south direction ($D_{NS} = 3 \times 10^4$ m) although there was no observational constraint in this direction. The effective duration time of heat/water discharge (t_d) is supposed to be ~ 10 h which is taken from the time from the onset to the peak of the initial temperature anomalies of GJT3 and TJT1 (Fig. 9). The water temperature anomaly in the affected region (ΔT_w) was overall $+0.1$ °C. Using specific heat ($C_w = 4 \times 10^3$ J/kg/°C) and density ($\rho_w = 10^3$ kg/m^3) of the typical seawater, the heat content (H) and the heat flux (Q) of the discharged water are, respectively, estimated to be:

$$H = C_w \rho_w D_{EW} D_{NS} h_w \Delta T_w \approx 4 \times 10^{16} \text{ J}, \qquad (2)$$

$$Q = H/t_d \approx 1 \times 10^{12} \text{ J/s}. \qquad (3)$$

Since the extension (i.e., volume) of the warm water spreading might not be well constrained as mentioned above, the estimation likely involves errors of about one order of magnitude. According to some studies (e.g., Baker et al. 1989; Lupton 1995; Lavell 1995), heat content and heat flux due to hydrothermal event plumes have been roughly 10^{15}–10^{17} J and 10^9–10^{11} J/s, respectively. The estimated heat properties of the warm water discharge immediately after the mainshock were comparable to those due to hydrothermal event plumes. These deep-sea transient heat events with such magnitudes would be related to anelastic subseafloor rupture and effective subseafloor fluid discharge to the seafloor.

A fault-valve model has been often employed to interpret a temporal evolution of fracture formation and associated fluid migration in the crust due to great earthquakes (Sibson et al. 1988; Sibson 1992). Sibson (2013) employed a fault-valve model for the M_w 9 mainshock.

We also suppose a similar fault-valve model in which the valve effectively opened to the seafloor in the large slip region and gradually closed. The exits of the fault valves could be mainly seafloor outcrops of the branch normal fault and those of the deeper faults (Fig. 12).

We consider the heat source which was responsible for the heat content of the discharged water (H). The heat source is mainly the geothermal fluids that were trapped within the branch normal fault and the deeper faults. Another possible source would be frictional heat generated by the mainshock slip at the plate boundary (e.g., Fulton et al. 2013).

We roughly examine whether the heat content of the geothermal fluids within the faults in the upper plate was almost responsible for H. For simplicity, we define that lengths of these faults are constant as l_f in the vertical direction from the seafloor, and that the total thickness of the permeable damage zones of these faults is d_f which is taken in the east–west direction (i.e., perpendicular to the trench axis). According to Fig. 12, $l_f = 3 \times 10^3$ m is supposed. The permeable fault damage zone indicates a fractured aquifer layer (e.g., Lockner et al. 2009; Faulkner et al. 2010; Hirose et al. 2021) whose porosity (ϕ) is supposed to be 10^{-1} (e.g., Tanikawa et al. 2014; Kameda et al. 2019). The typical geothermal gradient of $\nabla T_g = 0.03$ °C/m is assumed as mentioned above. Then, we suppose:

$$\begin{aligned} H &= C_w \rho_w D_{EW} D_{NS} h_w \Delta T_w \\ &= C_w \rho_w \phi d_f D_{NS} \nabla T_g \frac{1}{2} l_f^2, \end{aligned} \qquad (4)$$

or

$$d_f = 2 \frac{D_{EW} h_w \Delta T_w}{\phi \nabla T_g l_f^2} \approx 2 \times 10^1 \text{ m}. \qquad (5)$$

This thickness is composed of those major faults mentioned above (Fig. 12) and is roughly 10^0 m per fault.

The thickness of permeable fault damage zones has been known to widely range 10^{-1}–10^2 m (e.g., Moore and Shipley 1993; Savage and Brodsky 2011; Yehya et al. 2018). The estimated thickness of the multiple faults (d_f) and that of one fault roughly fall within this range. Thus, $H \approx 10^{16}$ J might be explained by that most of the geothermal fluids within the major faults in the upper plate were discharged to the seafloor. However, we remind that the estimation of d_f in Eq. (5) involves errors of one or two orders of magnitude since rough values were given especially for length and distance. It is not sure whether the frictional heat at the plate boundary during the mainshock effectively contributed to H.

In addition to JFAST, another future drilling project (JTRACK: Tracking the Tsunamigenic slips Across and Along the Japan Trench) proposed by IODP will be carried out at the mainshock epicentral seafloor (Kirkpatrick et al. 2015). Expected fault samples obtained there together with our temperature data will hopefully help to understand in detail the mainshock with related processes.

4.7 Subevents after the mainshock

The behaviors of the subevents of TJT1 (Fig. 10) are discussed. The temporal evolution of the temperature anomaly probably reflected the abrupt increase and decay of the warm water discharge, which also implied the opening and gradual closing of the fault valve. The temperature anomalies of GJT3 and TJT1 almost decayed over ~30 days but the decay behaviors were apparently different between them (Figs. 8 and 10). The decay of the temperature anomaly of GJT3 was relatively smooth. This indicated that the warm water ejection via the branch normal fault simply showed a smooth decay, or that the distance between GJT3 and the effective warm water exit along the outcrop of the branch normal fault might be large, and the warm water spreading might have substantially diffused at GJT3. Meanwhile, the temperature of TJT1 showed a complicated decay process (i.e., subevents). This indicated that the behaviors of the fault valves during the decay of the warm water discharges were probably different between the branch normal fault and the deeper seafloor faults.

The onsets of the subevents apparently occurred during low or falling tides (Fig. 10). The behaviors of the subevents are discussed more. There are possible differences between the fluid pathways near TJT1 in terms of material and mechanical properties. The reverse fault near TJT1 lies in the relatively consolidated crust. The backstop interface is an evident boundary between the consolidated crust and the unconsolidated (or weakly consolidated) frontal prism. There are also likely effective pathways in the unconsolidated frontal prism. Due to the large slip of the mainshock, pore fluid pressure in those pathways substantially changed locally near the plate boundary (Sibson 2013). Thermal pressurization below the frontal prism (e.g., Fulton et al. 2013) possibly facilitated fluid migration there. During the diminishing of these fluid pressure changes, substantial amounts of the subseafloor warm water in the multiple fault pathways likely migrated upward and approached close to the seafloor. Low or falling tidal loading possibly helped to unclamp the outcrops of the fault pathways so that the warm water near the seafloor ejected to the seafloor (Fig. 10c, d). The different timing of the onsets of the respective subevents might be attributed to possible differences in material and mechanical properties in the multiple fault pathways near TJT1. It is interesting that comparable phenomena of degassing at a cold seep and micro-earthquakes due to an impending eruption have been notably activated during low and/or falling tides in the deep seafloor (depths > ~1 km) conditions in which there are relatively small tidal variations of 10^1 hPa while the absolute pressure is greater than 10^5 hPa (e.g., Römer et al. 2016; Wilcock et al. 2016). We hope that the expected fault samples thanks to JTRACK will be utilized to understand the behaviors of subseafloor fluids after the mainshock as well as those during the mainshock.

5 Conclusions

Seafloor pressure observations were successfully carried out at eight stations above the hypocenter during the 2011 M_w 9 Tohoku earthquake and tsunami (Fig. 1). Temperature records from a built-in thermometer for thermal compensation of a quartz-crystal pressure transducer were used to estimate ambient water temperature. Using a heat conduction model, we proposed a method that the internal temperature record was reasonably converted to the time series of ambient water temperature both while the equipment was on the seafloor and while the equipment was floating up from the seafloor to the upper ocean (Figs. 2 and 3). This method was applied to the internal temperature data (Fig. 1 and Table 1).

The observational data showed remarkable temperature anomalies after the mainshock, which is described in Sect. 3.5. At deep seafloor stations of TJT1 and GJT3, there were abrupt water temperature increases of +0.10 °C and +0.20 °C, respectively, occurred several hours after the mainshock (Fig. 9). TJT1 showed intermittent temperature rises (i.e., subevents) for several days after the abrupt increase (Figs. 8 and 10). During the floating up of TJT1 2 weeks after the mainshock, the water temperature anomaly within +0.03 °C was found up to ~500 m above the seafloor (Fig. 11). The temperature anomaly of GJT3 became undetectable ~30 days after the mainshock (Fig. 7). P03 showed that an abrupt temperature increase of +0.19 °C occurred a few hours after the mainshock and terminated for several hours (Fig. 9). At the other five stations, there was no significant temperature anomaly related to the mainshock (Figs. 8 and 9).

We attempted to explain the water temperature anomalies. The temperature anomaly found at P03 was probably caused by the tsunami-generated turbidity current, as also studied by Arai et al. (2013). Considering the potential water temperature (Fig. 11) and the relationship between the temperature anomalies and the seafloor pressure variations (Fig. 10), we proposed a scenario that the initial temperature anomalies of TJT1/GJT3 and the following

Inazu *et al. Progress in Earth and Planetary Science*   (2023) 10:24

Page 23 of 27

subevents found at TJT1 were both caused by warm water discharges from subseafloor, rather than by turbidity currents due to tsunami or landslide (Fig. 12). The pathways of the warm water migration were the branch normal fault between GJT3 and TJT1, the reverse fault near TJT1, the backstop interface, and perhaps the several reverse faults at the frontal prism. The warm water discharges that caused the initial temperature anomalies of TJT1/GJT3 occurred within a few hours after the mainshock. The warm water ejection via the branch normal fault affected the temperature anomaly of GJT3 alone. The temperature anomalies of TJT1 including the subevents were affected by the warm water ejections via the multiple faults whose seafloor outcrops were close to TJT1 or located at depths deeper than TJT1. The spreading height of the discharged warm water was constrained by the height of neutral buoyancy (Figs. 11 and 12). The onsets of the warm water discharges to cause the following subevents of TJT1 were possibly helped by ocean tide loading reduction for several days after the mainshock (Fig. 10).

We confirmed that the scenario was mostly compatible with other geophysical (Tsuji et al. 2013; Park et al. 2021), geochemical (Kawagucci et al. 2012; Sano et al. 2014), and geological (Noguchi et al. 2012; Ikehara et al. 2021) observations that were carried out months after the mainshock. The anomalies captured by these post-mainshock surveys probably began with the initial temperature anomalies due to the warm water discharges which occurred within a few hours after the mainshock.

Based on the proposed scenario, we roughly estimated the heat source and the heat content which induced the observed water temperature anomalies, which possibly indicates that most of the warm water trapped within the major faults in the upper plate was discharged to the seafloor. The scenario with the heat estimation and the observed temperature data will be hopefully additional constraints on integrated modeling of the M_w 9 earthquake with surrounding phenomena with fine spatial–temporal resolution. The modeling includes not only the mainshock and aftershocks but also turbidity currents, water discharges with physical/chemical anomalies from the subseafloor, and resuspension/redistribution of seabed sediments. It is worthwhile to expect similar water temperature disturbances with complicated processes due to future giant earthquakes.

Abbreviations

M_w	Moment magnitude
CTD	Conductivity, temperature, and depth
JAMSTEC	Japan Agency for Marine-Earth Science and Technology
JFAST	Japan Trench Fast Drilling Project
IODP	Integrated Ocean Drilling Program
JTRACK	Tracking the Tsunamigenic slips Across and Along the Japan Trench

Availability of data and material

Please contact the corresponding author for data requests.

Declarations

Competing interests

The authors declare that they have no competing interest.

Author details

[1]Department of Marine Resources and Energy, Tokyo University of Marine Science and Technology, 4-5-7 Konan, Minato, Tokyo 108-8477, Japan. [2]Disaster Prevention Research Institute, Kyoto University, Gokasho, Uji, Kyoto 611-0011, Japan. [3]Research Center for Prediction of Earthquakes and Volcanic Eruptions, Graduate School of Science, Tohoku University, 6-6 Aza-Aoba, Aramaki, Aoba, Sendai 980-8578, Japan. [4]Kochi Institute for Core Sample Research (X-star), Japan Agency for Marine-Earth Science and Technology, 200 Monobe Otsu, Nankoku, Kochi 783-8502, Japan.

References

Arai K, Naruse H, Miura R, Kawamura K, Hino R, Ito Y, Inazu D, Yokokawa M, Izumi N, Murayama M, Kasaya T (2013) Tsunami-generated turbidity current of the 2011 Tohoku-Oki earthquake. Geology 41:1195–1198. https://doi.org/10.1130/G34777.1

Asano Y, Saito T, Ito Y, Shiomi K, Hirose H, Matsumoto T, Aoi S, Hori S, Sekiguchi S (2011) Spatial distribution and focal mechanisms of aftershocks of the 2011 off the Pacific coast of Tohoku earthquake. Earth Planets Space 63:669–673. https://doi.org/10.5047/eps.2011.06.016

Baker ET, Lavelle JW, Feely RA, Massoth GJ, Walker SL, Lupton JE (1989) Episodic venting of hydrothermal fluids from the Juan de Fuca Ridge. J Geophys Res Solid Earth 94:9237–9250. https://doi.org/10.1029/JB094iB07p09237

Becker K, Davis EE, Heesemann M, Collins JA, McGuire JJ (2020) A long-term geothermal observatory across subseafloor gas hydrates, IODP Hole U1364A Cascadia accretionary prism. Front Earth Sci 8:568566. https://doi.org/10.3389/feart.2020.568566

Bemis KG, Von Herzen RP, Mottl MJ (1993) Geothermal heat flux from hydrothermal plumes on the Juan de Fuca Ridge. J Geophys Res Solid Earth 98:6351–6365. https://doi.org/10.1029/92JB02273

Brodsky EE, Mori JJ, Anderson L, Chester FM, Conin M, Dunham EM, Eguchi N, Fulton PM, Hino R, Hirose T, Ikari MJ, Ishikawa T, Jeppson T, Kano Y, Kirkpatrick J, Kodaira S, Lin W, Nakamura Y, Rabinowitz HS, Regalla C, Remitti F, Rowe C, Saffer DM, Saito S, Sample J, Sanada Y, Savage HM, Sun T, Toczko S, Ujiie K, Wolfson-Schwehr M, Yang T (2020) The state of stress on the fault before, during, and after a major earthquake.

Annu Rev Earth Planet Sci 48:49–74. https://doi.org/10.1146/annurev-earth-053018-060507

Bryden HL (1973) New polynomials for thermal expansion, adiabatic temperature gradient and potential temperature of sea water. Deep Sea Res 20:401–408. https://doi.org/10.1016/0011-7471(73)90063-6

Chadwick WW Jr, Nooner SL, Butterfield DA, Lilley MD (2012) Seafloor deformation and forecasts of the April 2011 eruption at Axial Seamount. Nat Geosci 5:474–477. https://doi.org/10.1038/ngeo1464

Chester FM, Mori J, Eguchi N, Toczko S, Expedition 343/343T Scientists (2013) Expedition 343/343T summary. In: Proceedings of the IODP 343/343T. https://doi.org/10.2204/iodp.proc.343343T.101.2013

Clare M, Lintern DG, Rosenberger K, Hughes Clarke JE, Paull C, Gwiazda R, Cartigny MJB, Talling PJ, Perara D, Xu J, Parsons D, Jacinto RS, Apprioual R (2020) Lessons learned from the monitoring of turbidity currents and guidance for future platform designs. Geol Soc Spec Publ 500:605–634. https://doi.org/10.1144/SP500-2019-173

Dettmer J, Hawkins R, Cummins PR, Hossen J, Sambridge M, Hino R, Inazu D (2016) Tsunami source uncertainty estimation: the 2011 Japan tsunami. J Geophys Res Solid Earth 121:4483–4505. https://doi.org/10.1002/2015JB012764

Di Iorio D, Lavelle JW, Rona PA, Bemis K, Xu G, Germanovich LN, Lowell RP, Genc G (2012) Measurements and models of heat flux and plumes from hydrothermal discharges near the deep seafloor. Oceanography 25:168–179. https://doi.org/10.5670/oceanog.2012.14

Dietrich WE (1982) Settling velocity of natural particles. Water Resour Res 18:1615–1626. https://doi.org/10.1029/WR018i006p01615

Dobashi Y, Inazu D (2021) Improving detectability of seafloor deformation from bottom pressure observations using numerical ocean models. Front Earth Sci 8:598270. https://doi.org/10.3389/feart.2020.598270

Donohue KA, Watts DR, Tracey KL, Greene AD, Kennelly M (2010) Mapping circulation in the Kuroshio Extension with an array of current and pressure recording inverted echo sounders. J Atmos Ocean Technol 27:507–527. https://doi.org/10.1175/2009JTECHO686.1

Eble MC, González FI, Mattens DM, Milburn HB (1989) Instrumentation, field operations, and data processing for PMEL deep ocean bottom pressure measurements. NOAA Tech Memo ERL PMEL-89

Eble MC, Gonzalez FI (1991) Deep-ocean bottom pressure measurements in the Northeast Pacific. J Atmos Ocean Technol 8:221–233. https://doi.org/10.1175/1520-0426(1991)008%3c0221:DOBPMI%3e2.0.CO;2

Ekström G, Nettles M, Dziewoński AM (2012) The global CMT project 2004–2010: centroid-moment tensors for 13,017 earthquakes. Phys Earth Planet Int 200–201:1–9. https://doi.org/10.1016/j.pepi.2012.04.002

Faulkner DR, Jackson CAL, Lunn RJ, Schlische RW, Shipton ZK, Wibberley CAJ, Withjack MO (2010) A review of recent developments concerning the structure, mechanics and fluid flow properties of fault zones. J Struct Geol 32:1557–1575. https://doi.org/10.1016/j.jsg.2010.06.009

Fine IV, Kulikov EA, Cherniawsky JY (2013) Japan's 2011 tsunami: characteristics of wave propagation from observations and numerical modelling. Pure Appl Geophys 170:1295–1307. https://doi.org/10.1007/s00024-012-0555-8

Fox CG (1999) In situ ground deformation measurements from the summit of Axial Volcano during the 1998 volcanic episode. Geophys Res Lett 26:3437–3440. https://doi.org/10.1029/1999GL900491

Fujii Y, Satake K, Sakai S, Shinohara M, Kanazawa T (2011) Tsunami source of the 2011 off the Pacific coast of Tohoku earthquake. Earth Planets Space 63:815–820. https://doi.org/10.5047/eps.2011.06.010

Fujikura K, Kojima S, Tamaki K, Maki Y, Hunt J, Okutani T (1999) The deepest chemosynthesis-based community yet discovered from the hadal zone, 7326 m deep, in the Japan Trench. Mar Ecol Prog Ser 190:17–26. https://doi.org/10.3354/meps190017

Fujikura K, Fujiwara Y, Kojima S, Okutani T (2002) Micro-scale distribution of mollusks occurring in deep-sea chemosynthesis-based communities in the Japan Trench. Venus 60:225–236. https://doi.org/10.18941/venus.60.4_225

Fujimoto H (2014) Seafloor geodetic approaches to subduction thrust earthquakes. Monogr Environ Earth Planets 2:23–63. https://doi.org/10.5047/meep.2014.00202.0023

Fujimoto H, Hino R, Kido M, Ito Y, Ohta Y, Iinuma T, Osada Y, Inazu D, Suzuki S, Sato T, Tachibana K, Demachi T, Miura S (2014) Study of the 2011 off the Pacific coast of Tohoku earthquake based on seafloor and terrestrial geodetic observation. J Geod Soc Japan 60:1–22. https://doi.org/10.11366/sokuchi.60.1. (**in Japanese with English abstract**)

Fujiwara T, Kodaira S, No T, Kaiho Y, Takahashi N, Kaneda Y (2011) The 2011 Tohoku-Oki earthquake: displacement reaching the trench axis. Science 334:1240. https://doi.org/10.1126/science.1211554

Fukao Y, Kubota T, Sugioka H, Ito A, Tonegawa T, Shiobara H, Yamashita M, Saito T (2021) Detection of "rapid" aseismic slip at the Izu-Bonin Trench. J Geophys Res Solid Earth 126:e2021JB022132. https://doi.org/10.1029/2021JB022132

Fulton PM, Brodsky EE, Kano Y, Mori J, Chester F, Ishikawa T, Harris RN, Lin W, Eguchi N, Toczko S, Expedition 343, 343T, KR13-08 Scientists (2013) Low coseismic friction on the Tohoku-Oki fault determined from temperature measurements. Science 342:1214–1217. https://doi.org/10.1126/science.1243641

Fulton PM, Brodsky E, Mori JJ, Chester FM (2019) Tōhoku-oki fault zone frictional heat measured during IODP Expeditions 343 and 343T. Oceanography 32:102–104. https://doi.org/10.5670/oceanog.2019.129

Gaillard F, Autret E, Thierry V, Galaup P, Coatanoan C, Loubrieu T (2009) Quality control of large Argo datasets. J Atmos Ocean Technol 26:337–351. https://doi.org/10.1175/2008JTECHO552.1

Gibbs RJ, Matthews MD, Link DA (1971) The relationship between sphere size and settling velocity. J Sediment Petrol 41:7–18. https://doi.org/10.1306/74D721D0-2B21-11D7-8648000102C1865D

Gill AE (1982) Atmosphere-ocean dynamics. Academic Press, San Diego

Gomberg J, Ariyoshi K, Hautala S, Johnson HP (2021) The finicky nature of earthquake shaking-triggered submarine sediment slope failures and sediment gravity flows. J Geophys Res Solid Earth 126:e2021JB022588. https://doi.org/10.1029/2021JB022588

Gutscher M-A, Peacock SM (2003) Thermal models of flat subduction and the rupture zone of great subduction earthquakes. J Geophys Res Solid Earth 108:2009. https://doi.org/10.1029/2001JB000787

Hampton MA, Lee HJ, Locat J (1996) Submarine landslides. Rev Geophys 34:33–59. https://doi.org/10.1029/95RG03287

Hasegawa A, Yoshida K, Asano Y, Okada T, Iinuma T, Ito Y (2012) Change in stress field after the 2011 great Tohoku-Oki earthquake. Earth Planet Sci Lett 355–356:231–243. https://doi.org/10.1016/j.epsl.2012.08.042

Heerema CJ, Talling PJ, Cartigny MJ, Paull CK, Bailey L, Simmons SM, Parsons DR, Clare MA, Gwiazda R, Lundsten E, Anderson K, Maier KL, Xu JP, Sumner EJ, Rosenberger K, Gales J, McGann M, Carter L, Pope E, Monterey Coordinated Canyon Experiment (2020) What determines the downstream evolution of turbidity currents? Earth Planet Sci Lett 532:116023. https://doi.org/10.1016/j.epsl.2019.116023

Hino R, Ii S, Iinuma T, Fujimoto H (2009) Continuous long-term seafloor pressure observation for detecting slow-slip interplate events in Miyagi-Oki on the landward Japan Trench slope. J Disast Res 4:72. https://doi.org/10.20965/jdr.2009.p0072

Hino R, Inazu D, Ohta Y, Ito Y, Suzuki S, Iinuma T, Osada Y, Kido M, Fujimoto H, Kaneda Y (2014) Was the 2011 Tohoku-Oki earthquake preceded by aseismic preslip? Examination of seafloor vertical deformation data near the epicenter. Mar Geophys Res 35:181–190. https://doi.org/10.1007/s11001-013-9208-2

Hino R, Suzuki S, Kubota T, Ito Y, Fujimoto H (2012) Video image of seafloor near the epicenter of the 2011 Great Tohoku earthquake. Paper SSS39-P05 presented at JpGU Meeting 2012

Hino R, Ito Y, Ohta Y, Iinuma T, Inazu D (2013) Ocean bottom pressure records of the 2011 Tohoku-Oki earthquake. In: Proceedings of the 11th SEGJ International Symposium, pp 18–21. https://doi.org/10.1190/segj112013-117

Hirose T, Hamada Y, Tanikawa W, Kamiya N, Yamamoto Y, Tsuji T, Kinoshita M, Heuer VB, Inagaki F, Morono Y, Kubo Y (2021) High fluid-pressure patches beneath the décollement: a potential source of slow earthquakes in the Nankai Trough off Cape Muroto. J Geophys Res Solid Earth 126:e2021JB021831. https://doi.org/10.1029/2021JB021831

Hosoda S, Ohira T, Nakamura T (2008) A monthly mean dataset of global oceanic temperature and salinity derived from Argo float observations. JAMSTEC Rep Res Dev 8:47–59. https://doi.org/10.5918/jamstecr.8.47

Hughes Clarke JE (2016) First wide-angle view of channelized turbidity currents links migrating cyclic steps to flow characteristics. Nat Commun 7:11896. https://doi.org/10.1038/ncomms11896

Ide S, Tanaka Y (2014) Controls on plate motion by oscillating tidal stress: evidence from deep tremors in western Japan. Geophys Res Lett 41:3842–3850. https://doi.org/10.1002/2014GL060035

Iinuma T, Ohzono M, Ohta Y, Miura S (2011) Coseismic slip distribution of the 2011 off the Pacific coast of Tohoku earthquake (M 9.0) estimated based on GPS data—was the asperity in Miyagi-oki ruptured? Earth Planets Space 63:643–648. https://doi.org/10.5047/eps.2011.06.013

Iinuma T, Hino R, Kido M, Inazu D, Osada Y, Ito Y, Ohzono M, Tsushima H, Suzuki S, Fujimoto H, Miura S (2012) Coseismic slip distribution of the 2011 off the Pacific coast of Tohoku earthquake (M9.0) refined by means of seafloor geodetic data. J Geophys Res Solid Earth 117:B07409. https://doi.org/10.1029/2012JB009186

Ijiri A, Tsunogai U, Gamo T, Nakagawa F, Sakamoto T, Saito S (2009) Enrichment of adsorbed methane in authigenic carbonate concretions of the Japan Trench. Geo-Mar Lett 29:301–308. https://doi.org/10.1007/s00367-009-0143-9

Ikehara K, Kanamatsu T, Nagahashi Y, Strasser M, Fink H, Usami K, Irino T, Wefer G (2016) Documenting large earthquakes similar to the 2011 Tohoku-oki earthquake from sediments deposited in the Japan Trench over the past 1500 years. Earth Planet Sci Lett 445:48–56. https://doi.org/10.1016/j.epsl.2016.04.009

Ikehara K, Usami K, Irino T, Omura A, Jenkins RG, Ashi J (2021) Characteristics and distribution of the event deposits induced by the 2011 Tohoku-oki earthquake and tsunami offshore of Sanriku and Sendai, Japan. Sediment Geol 411:105791. https://doi.org/10.1016/j.sedgeo.2020.105791

Inazu D, Hino R, Fujimoto H (2012) A global barotropic ocean model driven by synoptic atmospheric disturbances for detecting seafloor vertical displacements from in situ ocean bottom pressure measurements. Mar Geophys Res 33:127–148. https://doi.org/10.1007/s11001-012-9151-7

Inazu D, Ikeya T, Waseda T, Hibiya T, Shigihara Y (2018) Measuring offshore tsunami currents using ship navigation records. Prog Earth Planet Sci 5:38. https://doi.org/10.1186/s40645-018-0194-5

Inoue T, Ito Y, Wallace LM, Yoshikawa Y, Inazu D, Garcia ESM, Muramoto T, Webb SC, Ohta K, Suzuki S, Hino R (2021) Water depth dependence of long-range correlation in nontidal variations in seafloor pressure. Geophys Res Lett 48:e2020GL092173. https://doi.org/10.1029/2020GL092173

Ito Y, Tsuji T, Osada Y, Kido M, Inazu D, Hayashi Y, Tsushima H, Hino R, Fujimoto H (2011) Frontal wedge deformation near the source region of the 2011 Tohoku-Oki earthquake. Geophys Res Lett 38:L00G05. https://doi.org/10.1029/2011GL048355

Ito Y, Hino R, Kido M, Fujimoto H, Osada Y, Inazu D, Ohta Y, Iinuma T, Ohzono M, Miura S, Mishima M, Suzuki K, Tsuji T, Ashi J (2013) Episodic slow slip events in the Japan subduction zone before the 2011 Tohoku-Oki earthquake. Tectonophysics 600:14–26. https://doi.org/10.1016/j.tecto.2012.08.022

Johnson HP, Gomberg JS, Hautala SL, Salmi MS (2017) Sediment gravity flows triggered by remotely generated earthquake waves. J Geophys Res Solid Earth 122:4584–4600. https://doi.org/10.1002/2016JB013689

Kakehi S, Narimatsu Y, Okamura Y, Yagura A, Ito S (2021) Bottom temperature warming and its impact on demersal fish off the Pacific coast of northeastern Japan. Mar Ecol Prog Ser 677:177–196. https://doi.org/10.3354/meps13852

Kameda J, Uno M, Conin M, Ujiie K, Hamada Y, Kimura G (2019) Fault weakening caused by smectite swelling. Earth Planets Space 71:131. https://doi.org/10.1186/s40623-019-1108-5

Kato A, Sakai S, Obara K (2011) A normal-faulting seismic sequence triggered by the 2011 off the Pacific coast of Tohoku earthquake: wholesale stress regime changes in the upper plate. Earth Planets Space 63:745–748. https://doi.org/10.5047/eps.2011.06.014

Kawagucci S, Yoshida-Takashima Y, Noguchi T, Honda MC, Uchida H, Ishibashi H, Nakagawa F, Tsunogai U, Okamura K, Takaki Y, Nunoura T, Miyazaki J, Hirai M, Lin W, Kitazato H, Takai K (2012) Disturbance of deep-sea environments induced by the M9.0 Tohoku earthquake. Sci Rep 2:270. https://doi.org/10.1038/srep00270

Kawamura K, Wada A, Römer M, Strasser M, Fink HG, Ito Y, Hino R (2021) Detailed seafloor observations on a deep-sea terrace along the Japan Trench after the 2011 Tohoku earthquake. In: Sassa K, Mikoš M, Sassa S, Bobrowsky PT, Takara K, Dang K (eds) Understanding and reducing landslide disaster risk. WLF 2020, ICL contribution to landslide disaster risk reduction, Springer, Cham, pp 405–410. https://doi.org/10.1007/978-3-030-60196-6_32

Kido M, Osada Y, Fujimoto H, Hino R, Ito Y (2011) Trench-normal variation in observed seafloor displacements associated with the 2011 Tohoku-Oki earthquake. Geophys Res Lett 38:L24303. https://doi.org/10.1029/2011GL050057

Kimura G, Hina S, Hamada Y, Kameda J, Tsuji T, Kinoshita M, Yamaguchi A (2012) Runaway slip to the trench due to rupture of highly pressurized megathrust beneath the middle trench slope: the tsunamigenesis of the 2011 Tohoku earthquake off the east coast of northern Japan. Earth Planet Sci Lett 339–340:32–45. https://doi.org/10.1016/j.epsl.2012.04.002

Kirkpatrick JD, Strasser M, Kodaira S, Sample J, Mori J, Saito S (2015) IODP workshop: tracking the Tsunamigenic slips across and along the Japan Trench (JTRACK). Sci Dril 19:27–32. https://doi.org/10.5194/sd-19-27-2015

Kodaira S, No T, Nakamura Y, Fujiwara T, Kaiho Y, Miura S, Takahashi N, Kaneda Y, Taira A (2012) Coseismic fault rupture at the trench axis during the 2011 Tohoku-oki earthquake. Nat Geosci 5:646–650. https://doi.org/10.1038/ngeo1547

Kodaira S, Nakamura Y, Yamamoto Y, Obana K, Fujie G, No T, Kaiho Y, Sato T, Miura S (2017) Depth-varying structural characters in the rupture zone of the 2011 Tohoku-oki earthquake. Geosphere 13:1408–1424. https://doi.org/10.1130/GES01489.1

Kodaira S, Fujiwara T, Fujie G, Nakamura Y, Kanamatsu T (2020) Large coseismic slip to the trench during the 2011 Tohoku-oki earthquake. Annu Rev Earth Planet Sci 48:321–343. https://doi.org/10.1146/annurev-earth-071719-055216

Kubota T, Hino R, Inazu D, Ito Y, Iinuma T, Ohta Y, Suzuki S, Suzuki K (2017) Coseismic slip model of offshore moderate interplate earthquakes on March 9, 2011 in Tohoku using tsunami waveforms. Earth Planet Sci Lett 458:241–251. https://doi.org/10.1016/j.epsl.2016.10.047

Kubota T, Saito T, Tsushima H, Hino R, Ohta Y, Suzuki S, Inazu D (2021) Extracting near-field seismograms from ocean-bottom pressure gauge inside the focal area: application to the 2011 Mw 9.1 Tohoku-Oki earthquake. Geophys Res Lett 48:e2020GL091664. https://doi.org/10.1029/2020GL091664

Lavelle JW (1995) The initial rise of a hydrothermal plume from a line segment source—results from a three-dimensional numerical model. Geophys Res Lett 22:159–162. https://doi.org/10.1029/94GL01463

Lavelle JW, Baker ET (1994) A numerical study of local convection in the benthic ocean induced by episodic hydrothermal discharges. J Geophys Res Oceans 99:16065–16080. https://doi.org/10.1029/94JC01203

Lienhard JH IV, Lienhard VJH (2003) A heat transfer textbook, 3rd edn. Phlogiston Press, Cambridge

Lin W, Conin M, Moore JC, Chester FM, Nakamura Y, Mori JJ, Anderson L, Brodsky EE, Eguchi N, Expedition 343 Scientists (2013) Stress state in the largest displacement area of the 2011 Tohoku-Oki earthquake. Science 339:687–690. https://doi.org/10.1126/science.1229379

Lockner DA, Tanaka H, Ito H, Ikeda R, Omura K, Naka H (2009) Geometry of the Nojima fault at Nojima-Hirabayashi, Japan–I. A simple damage structure inferred from borehole core permeability. Pure Appl Geophys 166:1649–1667. https://doi.org/10.1007/s00024-009-0515-0

Lupton JE (1995) Hydrothermal plumes: Near and far field. In: Humphris SE, Zierenberg RA, Mullineaux LS Thomson RE (eds) Seafloor hydrothermal systems: Physical, chemical, biological and geological interactions. AGU Geophys Monogr Ser 91. Washington, D.C., pp 317–346. https://doi.org/10.1029/GM091p0317

Macrander A, Böning C, Boebel O, Schröter J (2010) Validation of GRACE gravity fields by in-situ data of ocean bottom pressure. In: Flechtner F, Gruber T, Güntner A, Mandea M, Rothacher M, Schöne T, Wickert J (eds) System earth via geodetic-geophysical space techniques. Springer, Berlin, pp 169–185. https://doi.org/10.1007/978-3-642-10228-8_14

Matsumoto H, Araki E (2021) Drift characteristics of DONET pressure sensors determined from in-situ and experimental measurements. Front Earth Sci 8:600966. https://doi.org/10.3389/feart.2020.600966

McHugh CM, Kanamatsu T, Seeber L, Bopp R, Cormier M-H, Usami K (2016) Remobilization of surficial slope sediment triggered by the A.D. 2011

Mw 9 Tohoku-Oki earthquake and tsunami along the Japan Trench. Geology 44:391–394. https://doi.org/10.1130/G37650.1

McHugh CM, Seeber L, Rasbury T, Strasser M, Kioka A, Kanamatsu T, Ikehara K, Usami K (2020) Isotopic and sedimentary signature of megathrust ruptures along the Japan subduction margin. Mar Geol 428:106283. https://doi.org/10.1016/j.margeo.2020.106283

Mikada H, Mitsuzawa K, Matsumoto H, Watanabe T, Morita S, Otsuka R, Sugioka H, Baba T, Araki E, Suyehiro K (2006) New discoveries in dynamics of an M8 earthquake-phenomena and their implications from the 2003 Tokachi-oki earthquake using a long term monitoring cabled observatory. Tectonophysics 426:95–105. https://doi.org/10.1016/j.tecto.2006.02.021

Miura S, Takahashi N, Nakanishi A, Tsuru T, Kodaira S, Kaneda Y (2005) Structural characteristics off Miyagi forearc region, the Japan Trench seismogenic zone, deduced from a wide-angle reflection and refraction study. Tectonophysics 407:165–188. https://doi.org/10.1016/j.tecto.2005.08.001

Miura R, Hino R, Kawamura K, Kanamatsu T, Kaiho Y (2014) Accidental sediments trapped in ocean bottom seismometers during the 2011 Tohoku-Oki earthquake. Isl Arc 23:365–367. https://doi.org/10.1111/iar.12079

Moore G, Shipley T (1993) Character of the décollement in the Leg 131 area, Nankai Trough. In: Proceedings of the ocean drilling program, scientific results, pp 73–82

Murton BJ, Redbourn LJ (2000) Oceanographic evidence for a transient geothermal event affecting the Mid-Atlantic Ridge. Geophys Res Lett 27:1507–1510. https://doi.org/10.1029/1999GL002394

Noguchi T, Tanikawa W, Hirose T, Lin W, Kawagucci S, Yoshida-Takashima Y, Honda MC, Takai K, Kitazato H, Okamura K (2012) Dynamic process of turbidity generation triggered by the 2011 Tohoku-Oki earthquake. Geochem Geophys Geosyst 13:Q11003. https://doi.org/10.1029/2012GC004360

Nooner SL, Chadwick WW Jr (2009) Volcanic inflation measured in the caldera of Axial Seamount: implications for magma supply and future eruptions. Geochem Geophys Geosyst 10:Q02002. https://doi.org/10.1029/2008GC002315

Nosov MA, Kolesov SV (2007) Elastic oscillations of water column in the 2003 Tokachi-oki tsunami source: in-situ measurements and 3-D numerical modelling. Nat Hazards Earth Syst Sci 7:243–249. https://doi.org/10.5194/nhess-7-243-2007

Ogawa Y, Fujioka K, Fujikura K, Iwabuchi Y (1996) En echelon patterns of Calyptogena colonies in the Japan Trench. Geology 24:807–810. https://doi.org/10.1130/0091-7613(1996)024%3c0807:EEPOCC%3e2.3.CO;2

Oguri K, Kawamura K, Sakaguchi A, Toyofuku T, Kasaya T, Murayama M, Fujikura K, Glud RN, Kitazato H (2013) Hadal disturbance in the Japan Trench induced by the 2011 Tohoku-Oki earthquake. Sci Rep 3:1915. https://doi.org/10.1038/srep01915

Park J-O, Tsuru T, Fujie G, Hondori EJ, Kagoshima T, Takahata N, Zhao D, Sano Y (2021) Seismic reflection images of possible mantle-fluid conduits and basal erosion in the 2011 Tohoku earthquake rupture area. Front Earth Sci 9:687382. https://doi.org/10.3389/feart.2021.687382

Parker G, Fukushima Y, Pantin HM (1986) Self-accelerating turbidity currents. J Fluid Mech 171:145–181. https://doi.org/10.1017/S0022112086001404

Paull CK, Talling PJ, Maier KL, Parsons D, Xu J, Caress DW, Gwiazda R, Lundsten EM, Anderson K, Barry JP, Chaffey M, O'Reilly T, Rosenberger KJ, Gales JA, Kieft B, McGann M, Simmons SM, McCann M, Sumner EJ, Clare MA, Cartigny MJ (2018) Powerful turbidity currents driven by dense basal layers. Nat Commun 9:4114. https://doi.org/10.1038/s41467-018-06254-6

Polster A, Fabian M, Villinger H (2009) Effective resolution and drift of Paroscientific pressure sensors derived from long-term seafloor measurements. Geochem Geophys Geosyst 10:Q08008. https://doi.org/10.1029/2009GC002532

Römer M, Riedel M, Scherwath M, Heesemann M, Spence GD (2016) Tidally controlled gas bubble emissions: a comprehensive study using long-term monitoring data from the NEPTUNE cabled observatory offshore Vancouver Island. Geochem Geophys Geosyst 17:3797–3814. https://doi.org/10.1002/2016GC006528

Saffer DM, Tobin HJ (2011) Hydrogeology and mechanics of subduction zone forearcs: fluid flow and pore pressure. Annu Rev Earth Planet Sci 39:157–186. https://doi.org/10.1146/annurev-earth-040610-133408

Saito T, Ito Y, Inazu D, Hino R (2011) Tsunami source of the 2011 Tohoku-Oki earthquake, Japan: inversion analysis based on dispersive tsunami simulations. Geophys Res Lett 38:L00G19. https://doi.org/10.1029/2011GL049089

Saito T, Inazu D, Tanaka S, Miyoshi T (2013) Tsunami coda across the Pacific Ocean following the 2011 Tohoku-Oki earthquake. Bull Seismol Soc Amer 103:1429–1443. https://doi.org/10.1785/0120120183

Saito T, Baba T, Inazu D, Takemura S, Fukuyama E (2019) Synthesizing sea surface height change including seismic waves and tsunami using a dynamic rupture scenario of anticipated Nankai trough earthquakes. Tectonophysics 769:228166. https://doi.org/10.1016/j.tecto.2019.228166

Sano Y, Hara T, Takahata N, Kawagucci S, Honda M, Nishio Y, Tanikawa W, Hasegawa A, Hattori K (2014) Helium anomalies suggest a fluid pathway from mantle to trench during the 2011 Tohoku-Oki earthquake. Nat Commun 5:3084. https://doi.org/10.1038/ncomms4084

Sato M, Ishikawa T, Ujihara N, Yoshida S, Fujita M, Mochizuki M, Asada A (2011) Displacement above the hypocenter of the 2011 Tohoku-Oki earthquake. Science 332:1395. https://doi.org/10.1126/science.1207401

Savage HM, Brodsky EE (2011) Collateral damage: evolution with displacement of fracture distribution and secondary fault strands in fault damage zones. J Geophys Res Solid Earth 116:B03405. https://doi.org/10.1029/2010JB007665

Sequeiros OE, Mosquera RL, Pedocchi F (2018) Internal structure of a self-accelerating turbidity current. J Geophys Res Oceans 123:6260–6276. https://doi.org/10.1029/2018JC014061

Shanmugam G (2015) The landslide problem. J Palaeogeogr 4:109–166. https://doi.org/10.3724/SP.J.1261.2015.00071

Sibson RH (1992) Implications of fault-valve behaviour for rupture nucleation and recurrence. Tectonophysics 211:283–293. https://doi.org/10.1016/0040-1951(92)90065-E

Sibson RH (2013) Stress switching in subduction forearcs: implications for overpressure containment and strength cycling on megathrusts. Tectonophysics 600:142–152. https://doi.org/10.1016/j.tecto.2013.02.035

Sibson RH, Robert F, Poulsen KH (1988) High-angle reverse faults, fluid-pressure cycling, and mesothermal gold-quartz deposits. Geology 16:551–555. https://doi.org/10.1130/0091-7613(1988)016%3c0551:HARFFP%3e2.3.CO;2

Strasser M, Kölling M, Ferreira CDS, Fink HG, Fujiwara T, Henkel S, Ikehara K, Kanamatsu T, Kawamura K, Kodaira S, Römer M, Wefer G, R/V Sonne Cruise SO219A scientists, JAMSTEC Cruise MR12-E01 scientists (2013) A slump in the trench: Tracking the impact of the 2011 Tohoku-Oki earthquake. Geology 41:935–938. https://doi.org/10.1130/G34477.1

Sugawara D, Goto K (2012) Numerical modeling of the 2011 Tohoku-oki tsunami in the offshore and onshore of Sendai Plain, Japan. Sediment Geol 282:110–123. https://doi.org/10.1016/j.sedgeo.2012.08.002

Suzuki W, Aoi S, Sekiguchi H, Kunugi T (2011) Rupture process of the 2011 Tohoku-Oki mega-thrust earthquake (M9.0) inverted from strong-motion data. Geophys Res Lett 38:L00G16. https://doi.org/10.1029/2011GL049136

Suzuki S, Hino R, Kubota T, Ito Y, Inazu D (2015) Long-term continuous observation of vertical gradient of water temperature on the deep seafloor. Paper S31A-2734 presented at AGU Fall Meeting 2015

Talley LD, Pickard GL, Emery WJ, Swift JH (2011) Descriptive physical oceanography: an introduction, 6th edn. Elsevier, London. https://doi.org/10.1016/C2009-0-24322-4

Talling PJ, Wynn RB, Masson DG, Frenz M, Cronin BT, Schiebel R, Akhmetzhanov AM, Dallmeier-Tiessen S, Benetti S, Weaver PPE, Georgiopoulou A, Zühlsdorff C, Amy LA (2007) Onset of submarine debris flow deposition far from original giant landslide. Nature 450:541–544. https://doi.org/10.1038/nature06313

Talling PJ, Paull CK, Piper DJW (2013) How are subaqueous sediment density flows triggered, what is their internal structure and how does it evolve? Direct observations from monitoring of active flows. Earth Sci Rev 125:244–287. https://doi.org/10.1016/j.earscirev.2013.07.005

Tang L, Titov VV, Bernard EN, Wei Y, Chamberlin CD, Newman JC, Mofjeld HO, Arcas D, Eble MC, Moore C, Uslu B, Pells C, Spillane M, Wright L, Gica E (2012) Direct energy estimation of the 2011 Japan tsunami using deep-ocean pressure measurements. J Geophys Res Oceans 117:C08008. https://doi.org/10.1029/2011JC007635

Tanikawa W, Mukoyoshi H, Lin W, Hirose T, Tsutsumi A (2014) Pressure dependence of fluid transport properties of shallow fault systems in the Nankai subduction zone. Earth Planets Space 66:90. https://doi.org/10.1186/1880-5981-66-90

Tsuji T, Ito Y, Kido M, Osada Y, Fujimoto H, Ashi J, Kinoshita M, Matsuoka T (2011) Potential tsunamigenic faults of the 2011 off the Pacific coast of Tohoku earthquake. Earth Planets Space 63:831–834. https://doi.org/10.5047/eps.2011.05.028

Tsuji T, Kawamura K, Kanamatsu T, Kasaya T, Fujikura K, Ito Y, Tsuru T, Kinoshita M (2013) Extension of continental crust by anelastic deformation during the 2011 Tohoku-oki earthquake: the role of extensional faulting in the generation of a great tsunami. Earth Planet Sci Lett 364:44–58. https://doi.org/10.1016/j.epsl.2012.12.038

Tsuru T, Park J-O, Miura S, Kodaira S, Kido Y, Hayashi T (2002) Along-arc structural variation of the plate boundary at the Japan Trench margin: implication of interplate coupling. J Geophys Res Solid Earth 107:2357. https://doi.org/10.1029/2001JB001664

Usami K, Ikehara K, Jenkins RG, Ashi J (2017) Benthic foraminiferal evidence of deep-sea sediment transport by the 2011 Tohoku-oki earthquake and tsunami. Mar Geol 384:214–224. https://doi.org/10.1016/j.margeo.2016.04.001

Webb SC, Nooner SL (2016) High-resolution seafloor absolute pressure gauge measurements using a better counting method. J Atmos Ocean Technol 33:1859–1874. https://doi.org/10.1175/JTECH-D-15-0114.1

Wilcock WSD, Tolstoy M, Waldhauser F, Garcia C, Tan YJ, Bohnenstiehl DR, Caplan-Auerbach J, Dziak RP, Arnulf AF, Mann ME (2016) Seismic constraints on caldera dynamics from the 2015 Axial Seamount eruption. Science 354:1395–1399. https://doi.org/10.1126/science.aah5563

Xu JP, Sequeiros OE, Noble MA (2014) Sediment concentrations, flow conditions, and downstream evolution of two turbidity currents, Monterey Canyon, USA. Deep Sea Res 89:11–34. https://doi.org/10.1016/j.dsr.2014.04.001

Yamano M, Kawada Y, Hamamoto H (2014) Heat flow survey in the vicinity of the branches of the megasplay fault in the Nankai accretionary prism. Earth Planets Space 66:126. https://doi.org/10.1186/1880-5981-66-126

Yehya A, Yang Z, Rice JR (2018) Effect of fault architecture and permeability evolution on response to fluid injection. J Geophys Res Solid Earth 123:9982–9997. https://doi.org/10.1029/2018JB016550

Yilmaz M, Migliacio P, Bernard E (2004) Broadband vibrating quartz pressure sensors for tsunameter and other oceanographic applications. In: Proceedings of the Oceans 2004 Mar Technol Soc IEEE Techno-Ocean 2004, pp 1381–1387. https://doi.org/10.1109/OCEANS.2004.1405783

Zweng MM, Reagan JR, Seidov D, Boyer TP, Locarnini RA, Garcia HE, Mishonov AV, Baranova OK, Weathers K, Paver CR, Smolyar I (2019) World ocean atlas 2018, Salinity. NOAA Atlas NESDIS 82, vol 2. Silver Spring

Publisher's Note